

# Determination and quantification of sedimentary processes in salt marshes using end-member modelling of grain-size data

Nina Lenz<sup>1,2</sup>  | Sebastian Lindhorst<sup>1</sup>  | Helge W. Arz<sup>3</sup>

<sup>1</sup>Center for Earth System Research and Sustainability, CEN, Institute for Geology, Universität Hamburg, Hamburg, Germany

<sup>2</sup>Geomar, Helmholtz Centre for Ocean Research Kiel, Kiel, Germany

<sup>3</sup>Department of Marine Geology, Leibniz Institute for Baltic Sea Research Warnemünde (IOW), Rostock, Germany

## Correspondence

Sebastian Lindhorst, Center for Earth System Research and Sustainability, CEN, Institute for Geology, Universität Hamburg, Bundesstraße 55, 20146 Hamburg, Germany.  
Email: [sebastian.lindhorst@uni-hamburg.de](mailto:sebastian.lindhorst@uni-hamburg.de)

## Funding information

Deutsche Forschungsgemeinschaft, Grant/Award Number: Li2005/2-1 and 2-2

## Abstract

End-member modelling of bulk grain-size distributions allows the unravelling of natural and anthropogenic depositional processes in salt marshes and quantification of their respective contribution to marsh accretion. The sedimentology of two marshes is presented: (1) a sheltered back-barrier marsh; and (2) an exposed, reinstated foreland marsh. Sedimentological data are supplemented by an age model based on lead-210 decay and caesium-137, as well as geochemical data. End-member modelling of grain-size data shows that marsh growth in back-barrier settings is primarily controlled by the settling of fines from suspension during marsh inundation. In addition, nearby active dunes deliver aeolian sediment (up to 77% of the total sediment accretion), potentially enhancing the capability of salt marshes to adapt to sea-level rise. Growth of exposed marshes, by contrast, primarily results from high-energy inundation and is attributed to two sediment-transport processes. On the seaward edge of the marsh, sedimentation is dominated by coarser-grained traction load, whereas further inland, settling of fine-grained suspension load prevails. In addition, a third, coarse-grained sediment sub-population is interpreted to derive from anthropogenic land-reclamation measures, that is material from drainage channels relocated onto the marsh surface. This process contributed up to 34% to the total marsh accretion and terminated synchronously with the end of land reclamation measures. Data suggest that natural sediment supply to marshes alone is sufficient to outpace contemporary sea-level rise in the study area. This underlines the resilience potential of salt marshes in times of rising sea levels. The comparison of grain-size sub-populations with observed climate variability implies that even managed marshes allow for the extraction of environmental signals if natural and anthropogenic sedimentary processes are determined and their relative contribution to bulk sediment composition is quantified. Data series based solely on bulk sediments, however, seem to be of limited use because it is difficult to exclude bias of natural signals by anthropogenic measures.

This is an open access article under the terms of the [Creative Commons Attribution](https://creativecommons.org/licenses/by/4.0/) License, which permits use, distribution and reproduction in any medium, provided the original work is properly cited.

© 2022 The Authors. *The Depositional Record* published by John Wiley & Sons Ltd on behalf of International Association of Sedimentologists.

## KEYWORDS

climate archive, grain-size analysis, marsh sediments, North Sea, storm proxy

## 1 | INTRODUCTION

Salt marshes in north-western Europe develop along sheltered coastal segments, often associated with barrier islands, estuaries, embayments and coastal recesses (Dijkema, 1987). Salt-marsh growth is mainly controlled by tidal regime, inundation frequency, long-term sea level, and sediment availability (Allen & Pye, 1992; Fagherazzi et al., 2012; Pethick, 1981; Reed, 1990; Schuerch et al., 2012; Stevenson & Kearney, 2009). Vegetation plays a major role in marsh development as it stabilises deposited material and enhances further sedimentation by reducing the flow velocity during inundation (Boorman et al., 1998; Mudd et al., 2010). Marsh plants also directly contribute to marsh accretion by in-situ production of organic material (Allen, 2000).

Marshes are an important agent in coastal protection by attenuating storm waves (Möller, 2006). However, they are regarded as vulnerable to changes in tidal regime and storm activity, as expected in the course of global warming (Allen, 1995; Morris et al., 2002; Reed, 1995); their role in the context of coastal defence measures is therefore crucial. Recent studies predict accelerated drowning of marsh platforms and enhanced lateral erosion in the course of sea-level rise (Duarte et al., 2008; McFadden et al., 2007). In contrast to this global picture, many marshes at the North Sea coast appear more resilient to sea-level change and their total area increased in recent times; likely the result of more restrained marsh management (Stock et al., 2005; Wolff et al., 2010).

Salt marshes are able to adjust to sea-level rise as long as sediment supply is sufficient (Aranda et al., 2020; French, 1993; Kirwan & Temmerman, 2009; Kirwan et al., 2010). In this regard, Andersen et al. (2011) showed that salt marshes are threatened by sea-level rise if sediment supply is restricted and accretion remains unable to keep pace with increasing accommodation. Until now, the response of salt marshes to sea-level rise on longer time scales has been unclear (Kirwan & Megonigal, 2013), especially as many coasts are lined by dikes, preventing transgressive adaption of facies belts.

Salt marshes consist of clay-sized and silt-sized sediment with small amounts of sand and organic remnants (Bartholdy, 2012). The organic material is primarily autochthonous and consists of plant remains including their root networks (Allen, 2000). The relatively small grain size of marsh deposits results from suspension-dominated sediment transport during marsh inundation (Rahman & Plater, 2014).

Typical rates of marsh accretion along the North Sea coast are in the range of 1.9–20.3 mm year<sup>-1</sup> (Andersen et al., 2011; Butzeck et al., 2015). During the last millennium, coastal sedimentary dynamics in the southern North Sea experienced a profound modification in the course of coastal defence and the associated land reclamation by draining and dyking (Meier, 2004). The quantification of anthropogenic and natural sediment supply, and their respective contributions to marsh growth appear therefore vital for predictions on the future resilience of coastal marshes.

Marshes are primarily fed with sediment during inundation, making them potential recorders of storm climate. This even applies for reconstructions on the regional scale as storm-surge frequency in the North Sea is partly related to phase and strength of the North Atlantic Oscillation (NAO), with positive NAO phases triggering a northward shift of North Atlantic storm tracks and increased storm intensity and frequency in northern Europe (Dangendorf et al., 2012; Hurrell, 1995; Hurrell et al., 2003). The impact of NAO onto North Sea storm climate has been shown based on sea-level data (Dangendorf et al., 2012), and on high-resolution sedimentary archives like the sediments of coastal transgressive dunes, which show a multiannual variability in grain size, closely linked to storminess (Lindhorst & Betzler, 2016).

Grain size is an accepted proxy for the hydrodynamic conditions during transport and deposition, with coarser sediments generally indicating higher transport energy (Allen, 2000; Wheeler et al., 1998). Several studies consequently used the grain-size distribution of salt-marsh sediments to identify storm-surge deposits and to investigate the variability of local and regional storm climate (Andersen et al., 2011; Goodbred & Hine, 1995; Möller et al., 2014; Müller-Navarra et al., 2019; Reed, 1989; Schuerch et al., 2012; Stumpf, 1983; Swindles et al., 2018).

Storm-deposited sand beds in marshes, however, are often thin, which inhibits their identification based on discrete sediment samples. To overcome this issue, element distributions obtained from high-resolution X-ray fluorescence (XRF) core scanning have been proposed as proxy for grain size (Bunzel et al., 2021; Dypvik & Harris, 2001; Oldfield et al., 2003; van Hoang et al., 2010). However, the correlative link between storm climate and marsh accretion rate often remains ambiguous due to the multiplicity of sedimentary processes involved, the low generally temporal resolution of marsh records, and chronostratigraphic issues. A profound understanding

and unravelling of the different sedimentary processes involved in marsh accretion therefore appears essential. This can be achieved by deconvolving multi-modal grain-size distribution into subpopulations and by relating the respective end-members to depositional processes (Dietze et al., 2012). The approach that has been successfully applied to unravel sedimentary processes in different sedimentary environments (Dietze et al., 2014, 2021; Li et al., 2020; Patterson et al., 2020; Vauclin et al., 2021; Weltje, 1997; Weltje & Prins, 2003, 2007; Yang et al., 2020). Classical approaches to unravel mixed distributions, like method of moments, assume that the resulting parameters reflect the characteristics of the depositional environment (Friedman, 1967). This, however, only applies when the sediment sample comprises one unimodal size distribution. By contrast, end-member modelling analyses (EMMA), as applied in this study, allow for the mathematical decomposition of multi-modal (mixed source) distributions and the quantification of the resulting end-members (Dietze et al., 2012).

This study investigates the sedimentary record of two salt marshes that underwent different paths of development: A natural marsh located in a sheltered back-barrier setting and a former managed foreland marsh located in a higher-energy semi-enclosed embayment. The latter represents a typical setting along the North Sea coast, where marsh development, and as such the sedimentary record, is often altered by anthropogenic measures. The aim of this study is three-fold. First, characterisation of the main sedimentary processes that contribute to marsh growth. Second, quantification of their respective contribution to marsh accretion by using end-member modelling of grain-size data. A combination of surface samples (for characterising the recent sedimentary processes) and core data (to cover trends in the temporal domain) is used. Third, results of end-member modelling will be compared with time series from meteorological and tide-gauge observations to test the application of marsh sediments as record of storm climate.

## 2 | STUDY SITE

### 2.1 | Site 1 (Rantum Dunes)—a natural back-barrier salt-marsh

Site 1, Rantum Dunes, comprises a pristine natural-developed salt marsh on the barrier island of Sylt (southern North Sea; Figure 1). The study area is affected by a semidiurnal mesotidal regime (*sensu* Hayes, 1979), with a mean tidal range of 2 m (Kelletat, 1992; Puls et al., 2012). The nearest tide gauge, station ‘Hörnum Hafen’, has a mean high-water level (MHW) of 1.03 m

NHN (Normalhöhennull, the German reference datum), a mean low-water level (MLW) of  $-1.04$  m NHN and a mean high-water spring level (MHWS) of 1.26 m NHN (BSH, Bundesamt für Seeschifffahrt und Hydrographie). The western coast of the island of Sylt is exposed to high-energy waves from the North Sea and subject to coastal retreat (Lamprecht, 1957; Lindhorst et al., 2008). The back-barrier (eastern) coast, however, is sheltered and fringed by extensive salt marshes and tidal flats. The island comprises a sequence of coastal and transgressive dunes, largely stabilised by planting of heather and shrubs (Osswald et al., 2019).

The studied marsh faces the ‘Hörnum Basin’, a tidal bay, which is enclosed on three sides following the construction of a causeway, the ‘Hindenburg dam’, in 1927 CE (Figure 1). Since dam construction, water exchange with the open North Sea is restricted to a narrow tidal inlet south of the island and mud sedimentation increased (Wohlenberg, 1953).

The salt marsh of Rantum Dunes (Site 1) is located in a coastal pocket near the southern tip of Sylt (Figure 1B). Initiation of marsh development dates back to around 1915 CE (Schuerch et al., 2012). Nowadays, the marsh has a north–south extension of approximately 2800 m and a width between 60 and 240 m. The surface is flat and gently dips from 1.6 to 1.0 m NHN towards the tidal flat (Figure 1D). Despite its small dimensions, the vegetation zonation is typical of marshlands: The high marsh is dominated by *Juncus gerardii*, the low marsh by sea-purslane *Atriplex portulacoides*, and the pioneer marsh by the cord grass *Spartina anglica*. The transition from the pioneer marsh to the intertidal zone is a very low cliff (less than 15 cm high) and a jagged marsh boundary is present, typical for low-energy marshes (Leonardi & Fagherazzi, 2014).

### 2.2 | Site 2 (Bay of Tümlau)—a reinstated, former managed marsh

The salt marsh of Site 2 is a reinstated, formerly managed foreland marsh, located at the Bay of Tümlau (Eiderstedt Peninsula, Germany), a semi-enclosed tidal basin. The bay is partly protected from open North Sea waves by two intertidal to sub-tidal sandy shoals (Figure 1C; Hofstede, 1997). The area experiences semi-diurnal tides with a mean tidal range of 1.52 m (Müller-Navarra et al., 2016). Tidal data of the nearby tide gauge, station ‘Eider-Sperrwerk’, are MHW 1.52 m NHN, MLW  $-1.47$  m NHN and MHWS 1.6 m NHN (BSH).

The hinterland of the studied marsh was impoldered in 1933–1935 CE and subsequent ditching and dredging took place every 3–7 years (Müller-Navarra et al., 2016). Dredging of marsh channels was abandoned in 1985 CE,

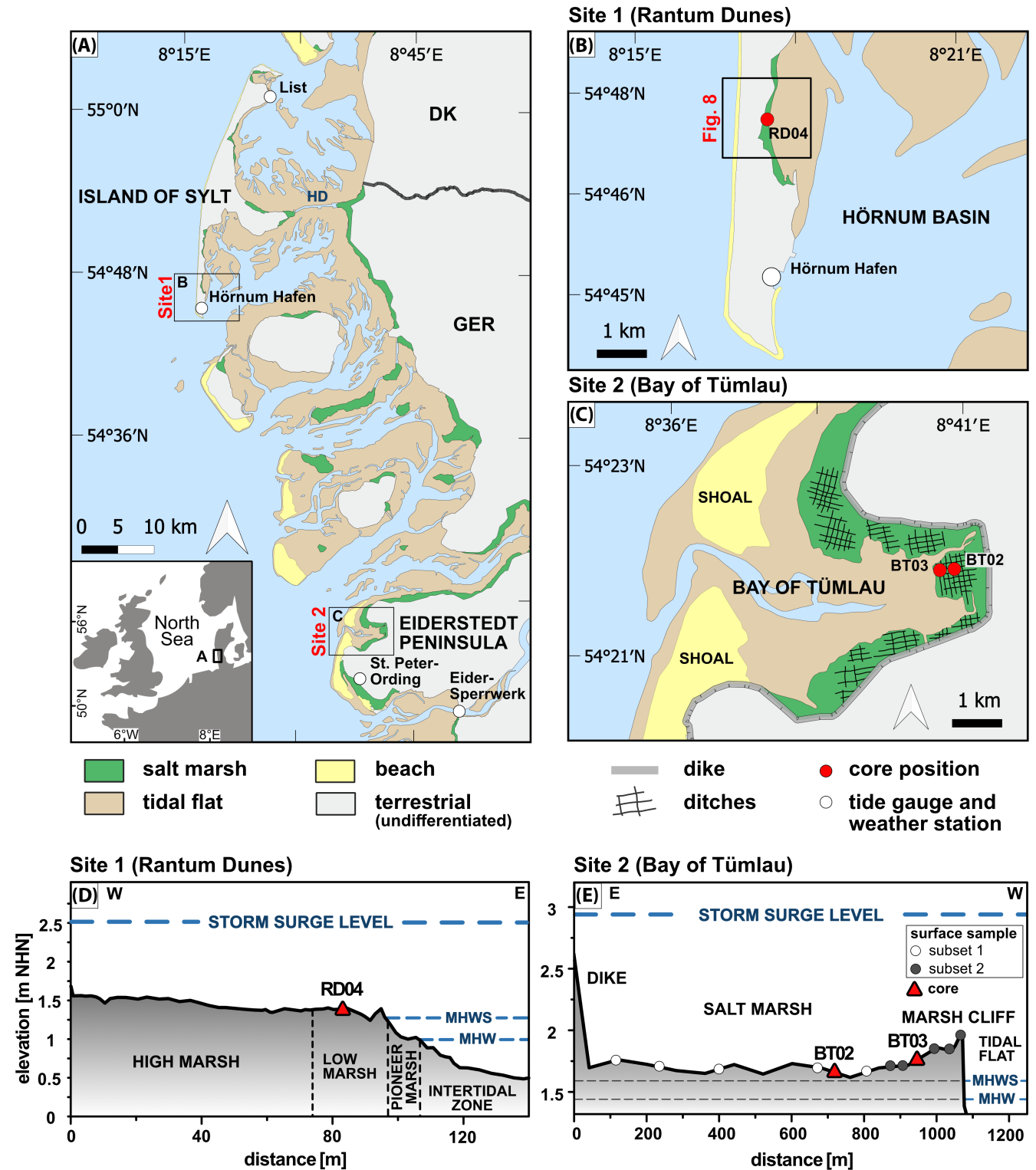


**FIGURE 1** (A) Location of study sites 1 (Rantum Dunes) and 2 (Bay of Tümlau), meteorological stations and tide gauges mentioned in the text. DK: Denmark; GER: Germany; HD: Hindenburg dam (B, C) Details of study sites 1 and 2 with core locations (D, E) Topographic, shore-normal cross sections of the studied marshes with water levels. Sea is right in both figures. MHWS, mean high-water spring level; MHW, mean high-water level.

with the foundation of the Wadden Sea National Park. Marsh ditching, the relocation of material from marsh channels to the marsh surface, however, continued until

1998 CE, when the area was declared a nature reserve (Stock et al., 2005). The pattern of artificial drainage channels still remains visible in the Bay of Tümlau, but



ditches have progressively filled with sediment. During the last decades, natural meandering channels evolved and the natural marsh vegetation re-established, with low-marsh plants *Triglochin maritima*, *A. portulacoides* and *Agrostis stolonifera*, together with few patches of high marsh vegetation like *Artemisia maritima* and *Halimone portulacoides*.

Today, the marsh is 1,080 m wide and surface elevation varies between 1.3 and 1.9 m NHN. The highest points are located at the seaward edge of the marsh and elevation decreases towards the dike (Figure 1E). The marsh edge shows a steep cliff in most parts which is vulnerable to lateral erosion and typical for high-energy settings (Mariotti & Fagherazzi, 2010). The present day salt-marsh edge is located above the MHWs, and in consequence is only inundated during storm surges.

### 3 | MATERIALS AND METHODS

#### 3.1 | Core recovery and on-site work

Three sediment cores were recovered from the salt-marshes at sites 1 and 2 (Figure 1; Table 1). Cores were obtained by means of PVC tubes with a diameter of 125 mm and a length of approximately 1.50 m; equipped with a steel core catcher. Tubes were manually hammered into the ground and recovered using a piston and a car lift. The method has been adapted from Besonen (2012).

Core RD04 recovered 0.94 m of undisturbed sediment from the low marsh at Rantum Dunes (Site 1; Figure 2A). Cores BT02 and BT03 recovered about 0.92 m each from locations 400 and 120 m from the seaward edge of the Bay of Tümlau salt marsh (Site 2; Figure 3A,B). Core positions align along a coast-normal transect to account for changes in the sedimentary framework conditions with varying distance to the marsh edge. Sediment compaction resulting from coring was calculated as the differences between the sediment surface inside and outside of the coring tube after the target depth has been reached; compaction was a maximum of 1.3% and is therefore regarded as negligible (Table 1).

Surface sediment samples (1.5 cm<sup>3</sup> each) were also taken from the salt marsh of Site 2 (Bay of Tümlau) two

days after a storm surge (water level 2.66 m above mean high water) on 12 February 2020 CE (for sample locations see Figure 1E). Surface sediments were sampled along a coast-normal transect to cover the range of marsh zones and to better elucidate trends in grain-size resulting from varying hydrodynamic conditions (Collins et al., 1987; de Groot et al., 2011; Yang et al., 2008).

Core locations and surface elevations were measured by means of a Leica GS09 RTK GPS (spatial accuracy better than 0.02 m in all three axes, manufacturer specifications) and a Leica NA700 optical theodolite.

#### 3.2 | Grain-size analyses and end-member modelling

Cores were split and sampled equidistantly for grain-size analyses (1.5 cm<sup>3</sup> each 1 cm). Samples were treated with 10%–30% hydrogen peroxide and 60% acetic acid to dissolve organic and carbonate phases. Prior to grain-size measurement, samples were suspended in water using tetra-sodium diphosphate decahydrate as a dispersing agent. Grain-size distributions were determined with a laser-diffraction particle-sizer (Sympatec HELOS/KF Magic; range 0.5/18 to 3200 μm, 32 grain-size classes). To ensure accuracy of measurements, an in-house grain-size standard was measured daily (standard deviation <3.3 μm). Grain-size statistics are based on the graphical method (Folk & Ward, 1957), calculated using Gradistat (Blott & Pye, 2001). Grain-size values were rounded to the next integer for use in the text.

Grain-size distributions were used as input for end-member modelling using the R package EMMAgeo (Dietze & Dietze, 2016, 2019; Dietze et al., 2012; EMMAgeo version 0.9.7; R version 4.2.0). Results of EMMA are so-called ‘loadings’, which represent the end-members of the respective grain-size spectrum. ‘Scores’ represent the contribution of each end-member to the bulk-sediment composition. (Dietze & Dietze, 2019; Dietze et al., 2012). Robust end-members were calculated by applying the compact protocol of robust EMMA, which yield the uncertainty estimates of end-members. The optimal number of end-members

**TABLE 1** Meta data of sediment cores used for this study. ‘Compaction by coring’ refers to the reduction in total sediment thickness due to the process of core recovery; compare methods.

Core		Core location			Coring date	Compaction by coring	
ID	Length (cm)	Site	Lat. (°)	Lon (°)		cm	%
RD04	32	1, Rantum Dunes	54.787686	8.291476	2019-03-27	0.5	0.5
BT02	92	2, Bay of Tümlau	54.364871	8.682585	2020-02-14	0.4	0.4
BT03	93	2, Bay of Tümlau	54.364652	8.678139	2020-02-14	1.2	1.3

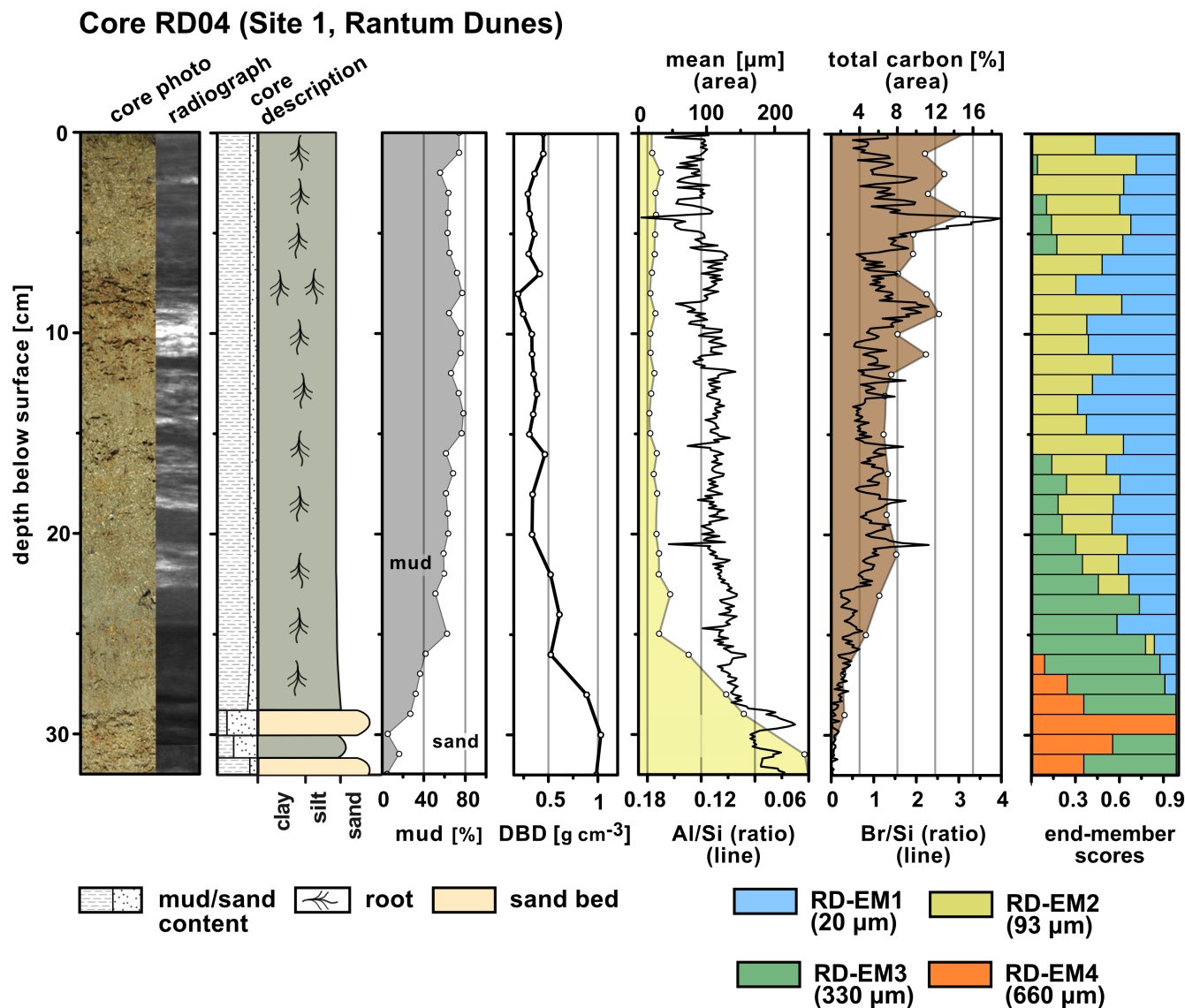


**FIGURE 2** Sedimentology of core RD04 (Site 1, Rantum Dunes; see Figure 1 for location) and results of end-member modelling of grain-size data. DBD, dry bulk density; Al/Si, Br/Si, element ratios calculated from X-ray fluorescence core scanning data.

were determined of mean total, samples-wise as well as class-wise  $R^2$  between the original data set and the modelled data set. The evaluation of overlapping end-member loadings was used as a further validation criterion. Grain-size class limits were defined by the identification of plausible loadings based on all possible model scenarios. Since the scores represent the relative contribution of the respective end-members to bulk-sediment composition, sedimentation rates for individual end-members were computed by multiplying the total sedimentation rate with the respective scores. Subsequently, grain-size statistics of distinct end-members were re-calculated to characterise the specific sediment sub-population.

End-member modelling for Site 2 (Bay of Tümlau) is based on separate analyses of each core and the surface

samples, in order to minimise the impact of local effects like, for example, the distance to the marsh edge. In this regard, it is assumed that salt-marsh sediments may gradually fine from the marsh edge to their landward termination due to decreasing transport energy. The algorithm EMMA aims to unmix robust end-members and consequently fails if grain-size data are afflicted with a trend (Dietze et al., 2021; Weltje, 1997). To account for this, samples of the recent storm surge sediments were split into two data subsets. Subset 1 represents surface sediments sampled near the marsh edge and subset 2 contains samples from more landward localities (Figure 1). To test the stability of the analysis, end-member calculation was also performed based on a pooled sample set at Site 2: all samples from Site 2, including core BT02, BT03 and surface samples (Figure S1).

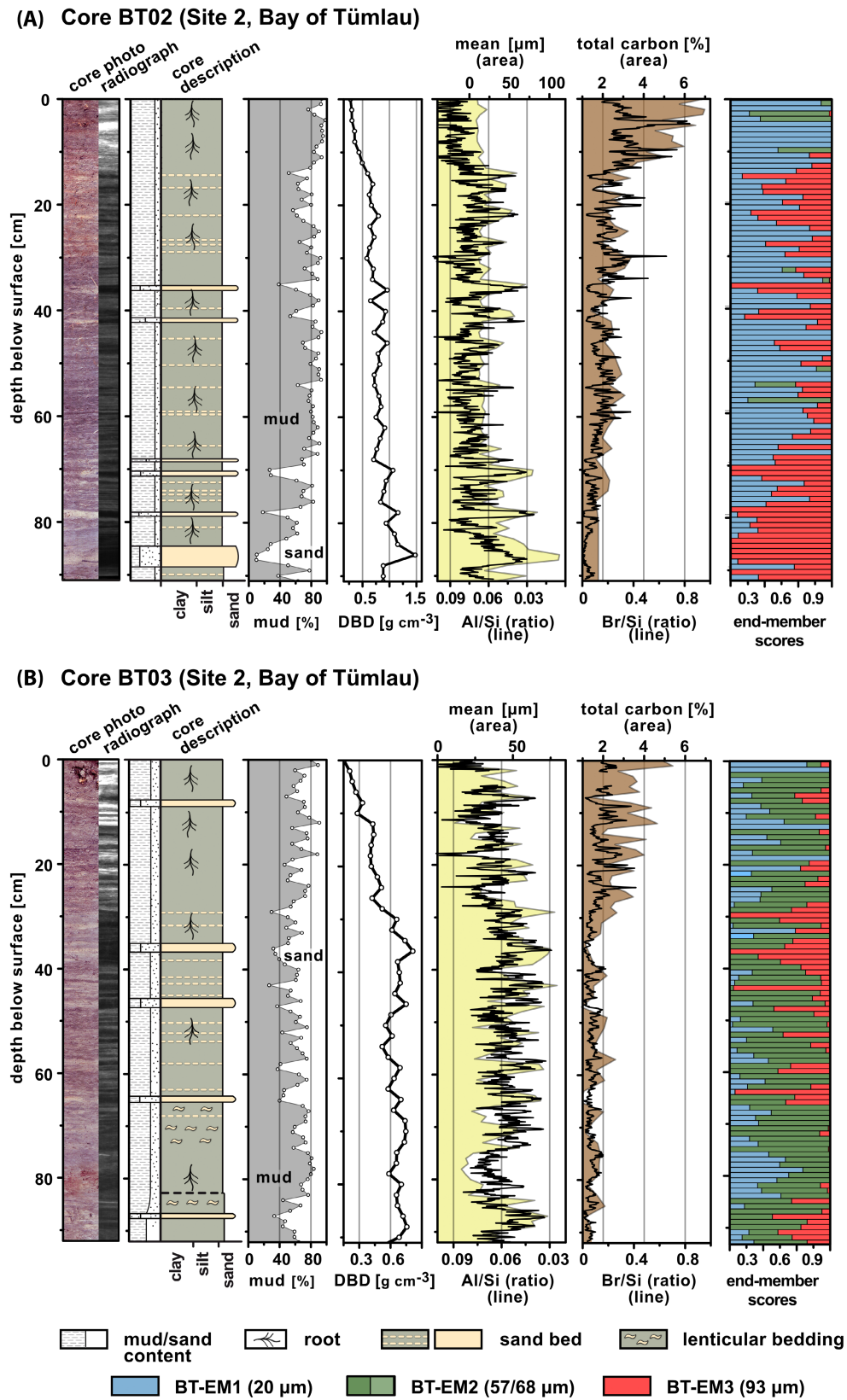


**FIGURE 3** Sedimentology of cores BT02 and BT03 (Site 2, Bay of Tümlau; see Figure 1 for location) and results of end-member modelling of grain-size data. DBD: dry bulk density; Al/Si, Br/Si: element ratios calculated from X-ray fluorescence core scanning data.

### 3.3 | Carbon content, dry bulk density and sediment autocompaction

Samples for the determination of carbon content were taken equidistantly (1.5 cm<sup>3</sup> each 1 cm in the uppermost 30 cm of the cores and each 2 cm further downcore). Sample preparation included freeze drying and hand crushing of the sediment to silt size. Carbon content was measured using a LECO SC-144 DR carbon analyser.

The *in situ* dry bulk density (DBD) was calculated by dividing the mass of the dry samples by their wet volume, following the approach of Avnimelech et al. (2001). To confirm DBD values, bulk densities were also calculated from water content and total carbon content (assumed to equal organic carbon due to the absence of shells), after Kolker et al. (2009). Results of both approaches correlate well ( $r = 0.90$ ;  $p < 0.01$ ; all correlations calculated using Spearman's rank correlation; Zar, 2005), and DBD values are therefore regarded as reliable. Down-core dry bulk densities were estimated based on the DBD of the uppermost 0.05 m following Bartholdy et al. (2010), and used to correct measured sediment thicknesses for autocompaction. These data were used for the calculation of sedimentation rates.

### 3.4 | XRF core scanning and radiographs

Core logging was carried out at the Leibniz Institute for Baltic Sea Research Warnemünde (IOW) using an ITRAX XRF core scanner with a high-power chromium-XRF source. All cores were scanned with a down-core resolution of 1 mm, 30 kV source voltage, a current of 55 mA and 5 s measuring time per step. Results were regarded as valid, with exception of parts of core BT03, which showed exceptionally high argon counts for the depth interval 2–5 cm, visually correlated with cracks in the sediment surface. This interval was excluded from further analysis. Radiographs were obtained using 60 kV, a current of 30 mA and 1,300 ms measuring time. They are represented as grey-scale images with lighter colour coding higher X-ray intensities (i.e. more organic) and darker intervals reflecting a higher attenuation of X-rays (i.e. less organic material, higher sand content).

### 3.5 | Radionuclides and age model

Analysis of radionuclides for age determination based on the decay of lead-210 was conducted at Flett Research Ltd (Canada) using alpha spectrometry. The isotopes <sup>209</sup>Po, <sup>210</sup>Po and <sup>226</sup>Ra were measured for 2 cm thick sediment intervals to calculate the activity of supported and unsupported <sup>210</sup>Pb (see Pittauerova et al., 2011 for details on method).

Polonium isotopes <sup>209</sup>Po and <sup>210</sup>Po were measured for 20 intervals in core in RD04 (0–32 cm core depth), 15 intervals in core BT02 (0–90 cm) and 14 intervals in core BT03 (0–92 cm), with a down-core decrease in sampling resolution. Measurements on <sup>137</sup>Cs activity were carried out for seven intervals in core RD04 (11–26 cm), 17 intervals in core BT02 (6–62 cm) and 14 intervals in core BT03 (18–60 cm).

The constant rate of supply model (CRS; Goldberg, 1963) was applied to calculate sedimentation rates for cores RD04 and BT03 (Figure 4). The CRS model accepts changes in sedimentation rate but assumes a constant atmospheric input of <sup>210</sup>Pb (Appleby et al., 1990). Calculated sedimentation rate is high, when the activity of unsupported <sup>210</sup>Pb is low and vice versa. For core RD04, a linear regression model was applied to estimate an average sedimentation rate, which was then used to calibrate the CRS model.

Core BT02 shows a rapid decrease in lead-210 activity in the depth interval 8–23 cm. This prevents the application of the CRS model, which assumes a predictable decrease in <sup>210</sup>Pb content with depth. This is the case for BT02 core intervals 0–8 cm and 23–60 cm, which enables the application of two independent linear regression models for these intervals. Age model and averaged sediment-accumulation rates were further improved by using <sup>137</sup>Cs marker horizons.

Error bars for radionuclide activity are based on Gaussian error propagation and provided with one sigma standard deviation. Errors for sediment ages were calculated following the approach of Binford (1990). All ages in the text were rounded to the next integer.

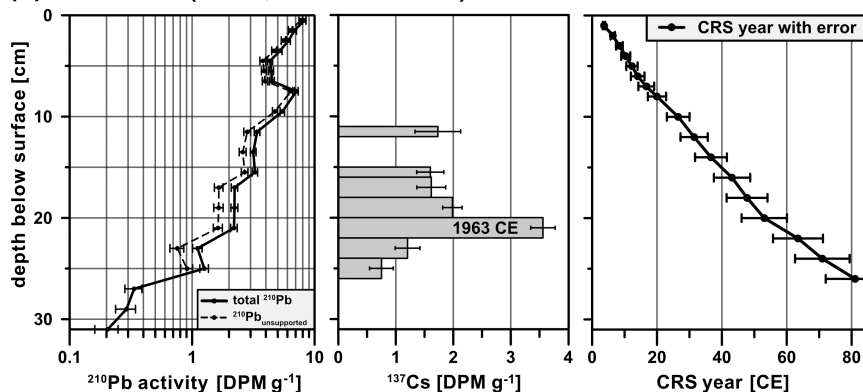
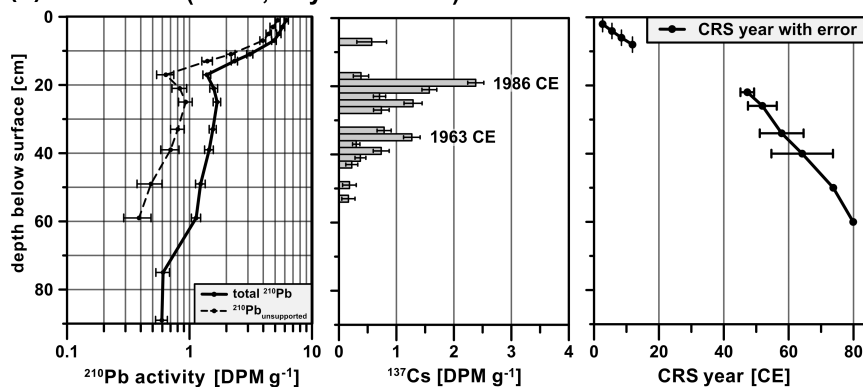
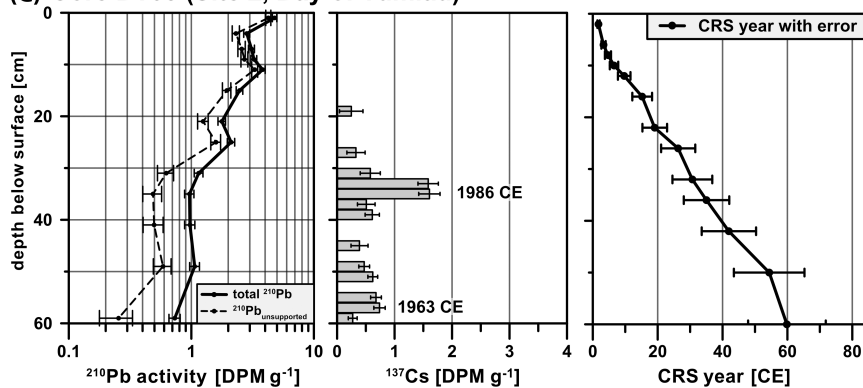
### 3.6 | Tide-gauge and meteorological data

Daily high-water levels from tide gauges 'Hörnnum Hafen' (54.758113°N/8.29606°E; 3 km south of Site 1; Figure 1), and 'Eider-Sperrwerk' (54.265963°N/8.841937°E; 15 km south of Site 2) were provided by the Wasserstraßen- und Schifffahrtsamt Tönning, Germany. Data cover the time periods 1936–2018 CE (Hörnnum Hafen) and 1972–2018 CE (Eider-Sperrwerk), respectively.

Storm-surge frequency, that is water levels exceeding 1.5 m above MHW, is characterised by the annual number of storm surges; flooding intensity is represented by the annual mean inundation height of the marsh (following Schuerch et al., 2012). The relative mean sea level of Cuxhaven (53.876518°N/8.699112°E) was used as the reference for long-term trends in high-water level (after Wahl et al., 2010).

Time series on wind are from the Climate Data Center (CDC) of the Deutscher Wetterdienst (DWD, German National Meteorological Service). Data for stations 'List' in Sylt (27 km north of Site 1; Figure 1A) and 'St. Peter-Ording' (7 km south of Site 2) cover the time periods 1937–2018 CE



**(A) Core RD04 (Site 1, Rantum Dunes)****(B) Core BT02 (Site 2, Bay of Tümlau)****(C) Core BT03 (Site 2, Bay of Tümlau)**

**FIGURE 4** (A–C) Results of lead-210 and caesium-137 measurements, as well as CRS (constant rate of supply) age models for cores RD04 (A), BT02 (B) and BT03 (C). See Figure 1 for core locations and text for data description and discussion.

and 1975–2018 CE (with years 1982 and 1983 CE missing), respectively. Hourly observations of mean wind direction and daily maximum wind gusts were used to derive the annual number of westerly winds exceeding 6 Bft ( $10.8 \text{ m s}^{-1}$ ).

## 4 | RESULTS

### 4.1 | Sedimentology

#### 4.1.1 | Site 1, Rantum Dunes (core RD04)

Core RD04 recovered a succession of silt and clay (mud content up to 78% with intercalated sandy layers;

Figure 2). The sediment is grey-brown and root fragments are persistent in the uppermost 28 cm. No mollusc shells were found. Sediment fines upward from the bottom of the core to around 22 cm core depth, and subsequently remains in the clay to fine-silt range until the modern surface. Visual core inspection shows two distinct sand layers at 32 and 28 cm core depth. Radiographs reveal more subtle changes in sediment composition, including pronounced radiographically less dense intervals (lighter colours) in the middle part of the core (between 22 and 10 cm). The lowermost part of the core, by contrast, is composed of radiographically more dense material (dark), especially below 25 cm core depth. This correlates with very low mud

contents. Mean grain size ranges from 16 to 788  $\mu\text{m}$ , but remains between 16 and 33  $\mu\text{m}$  in the uppermost 22 cm. The size of the largest sediment grains, as represented by the  $d_{90}$  of the grain-size distributions, is between 150 and 800  $\mu\text{m}$  (see [Figure S1](#)). Sediment sorting of all samples is extremely poor (1.6–8.2 phi, see [Figure S1](#)) and grain-size distributions are strongly negatively skewed (−0.3 to −0.6 phi).

The total carbon content of core RD04 sediments increases from 0.8% to 15% towards the modern surface ([Figure 2](#)). The DBD varies between 0.19 and 1.03  $\text{g cm}^{-3}$  and is highest in the lowermost part of the core. Visually, there is a correlation with the sediment grain size, with higher DBDs correlating with coarser sediments.

Chemical composition of RD04 sediments, as retrieved from XRF core scanning, is highly variable at the millimetre scale ([Figure 2](#)). The Al/Si ratio shows a subtle down-core trend towards lower values, which becomes obvious for core depths exceeding 26 cm. Correlation between Al/Si ratios and mean grain size is strongly negative ( $r = -0.70$ ;  $p < 0.05$ ). The Br/Si ratio is variable in the upper 20 cm of core RD04 and decreases with greater depths. Correlation between the Br/Si ratio and total carbon content is positive ( $r = 0.63$ ;  $p < 0.05$ ).

#### 4.1.2 | Site 2, Bay of Tümlau (cores BT02, BT03 and surface samples)

Cores BT02 and BT03 recovered a grey-brown fine-grained sediment. Root fragments are persistent in the upper 80 cm of both cores, and no mollusc shells were found. Sediments are clay and silts, with higher mud contents in core BT02 ([Figure 3](#)). Both cores show intercalated sand layers, between one millimetre and several centimetres thick ([Figure 3](#)). While the thinner sand layers are difficult to recognise visually, radiographs clearly show them below 15 cm depth in core BT02, and below 14 cm depth in core BT03. Sand content in these layers is up to 90% in core BT02 and up to 73% in core BT03.

The grain-size distributions are symmetrical to strongly negatively skewed (−0.6 to 0.0 phi, see [Figure S1](#)) and sediment is poorly to extremely poorly sorted (BT02: 1.4–9.5 phi; BT03: 1.5–5.3 phi). The mean grain size of core BT02 sediments varies between 8 and 113  $\mu\text{m}$ , but generally remains  $<25 \mu\text{m}$  ([Figure 3A](#)). At core depths exceeding 15 cm, grain-size shows several coarse peaks associated with the sand layers. Coarsest sediments are at the bottom of the core, below 65 cm. In core BT03, mean grain size varies between 12 and 79  $\mu\text{m}$ , but generally is  $<50 \mu\text{m}$  ([Figure 3B](#)). In this core, there are more sand layers compared to core BT02, and lenticular bedding occurs at core depths  $>65 \text{ cm}$ .

Recent storm-surge deposits have a mean grain size between 8 and 55  $\mu\text{m}$  and contain up to 99.5% mud ([Figure S1](#)). Surface sediment of the tidal flat in front of the marsh has a mean grain size of 44–89  $\mu\text{m}$  and a sand content of up to 78%.

The total carbon content increases towards the surface from 1.4% to 7% in core BT02, and from 0.8% to 5.4% in core BT03; the highest values occur in the uppermost 15 cm in core BT02 and in the uppermost 25 cm in core BT03. The DBD decreases up-core from 1.49 to 0.28  $\text{g cm}^{-3}$  in core BT02, and from 0.81 to 0.15  $\text{g cm}^{-3}$  in core BT03 ([Figure 3](#)).

The Al/Si ratios of cores BT02 and BT03 exhibit pronounced changes on the centimetre scale, which visually correlates with sand layers ([Figure 3](#)). Correlation between Al/Si ratios and mean grain size is negative (BT02:  $r = -0.79$ ;  $p < 0.05$ ; BT03:  $r = -0.59$ ;  $p < 0.05$ ). The Br/Si ratio decreases with depth and correlation between Br/Si ratios and total carbon content is consequently high (BT02:  $r = 0.71$ ;  $p < 0.05$ ; BT03:  $r = 0.63$ ;  $p < 0.05$ ).

## 4.2 | End-member modelling of grain-size distributions

### 4.2.1 | Site 1, Rantum Dunes (core RD04)

End-member modelling results of RD04 grain-size data revealed a minimum number of four and a maximum of five potential end-members ([Figure S2](#)). To account for the overlap of sub-populations in the coarse range, four end-members (EM) have been selected for best performance ([Figure S2](#)). These sub-populations of core RD04 sediments, namely RD-EM1, RD-EM2, RD-EM3 and RD-EM4 are characterised by dominant modes at 20, 93, 330 and 660  $\mu\text{m}$  ([Figure 5A](#)). Grain-size class limits were defined as 10–40, 60–130, 200–400 and 500–1000  $\mu\text{m}$  for end-members EM1, EM2, EM3 and EM4, respectively. Data show a class-wise explained variance of 89% and a sample-wise explained variance of 86% ([Figure S2](#)). The relative contribution of grain-size sub-populations to the bulk sediment composition of core RD04 (represented by the scores) is 20%, 21%, 27% and 32% for RD-EM1, RD-EM2, RD-EM3, and RD-EM4, respectively ([Figure 2](#)). Sediments assigned end-member RD-EM4 only occur in the lowermost part of the core, below 27 cm core depth, correlating with the sand layers ([Figure 2](#)).

### 4.2.2 | Site 2, Bay of Tümlau (storm surge deposits BT-SF, cores BT02 and BT03)

The recent storm-surge sediments from Site 2 were split into two subsets (see methods). Subset 1 reveals a

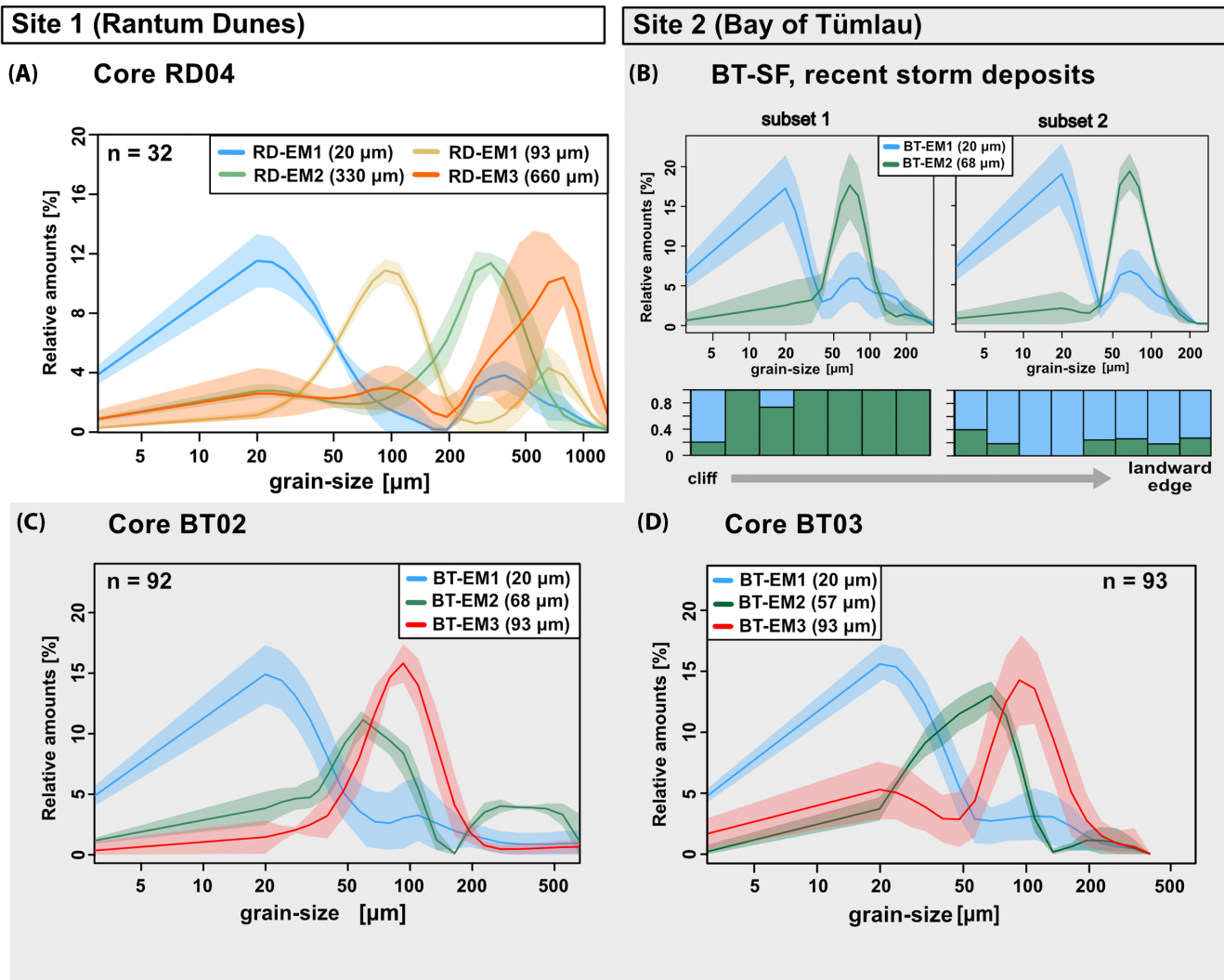


**FIGURE 5** Results of end-member modelling of grain-size distributions for (A) Core RD04 (Site 1, Rantum Dunes); (B) Surface samples (BT-SF) of storm surge deposits (Site 2, Bay of Tümlau; see [Figure 1E](#) for sample locations), bar chart gives relative portion of sediments assigned to end-members SF-EM1 and SF-EM2, respectively; and (C, D) Cores BT02 and BT03 (Site 2, Bay of Tümlau).

minimum number of two and a maximum number of three potential end-members ([Figure S5](#)). Two of these overlap in the size range 40–120  $\mu\text{m}$  and are interpreted as similar. Based on all plausible loadings, class limits were defined as 5–30 and 50–120  $\mu\text{m}$  for the remaining two end-members ([Figure S5](#)); dominant modes are at 20 and 68  $\mu\text{m}$  ([Figure 5A](#)). The relative contribution of subset 1 end-members to the bulk-sample composition is 84 and 16% ([Figure S5](#)). Subset 2 reveals similar plausible loadings with same mode positions and class limits of 5–40 and 50–150  $\mu\text{m}$  ([Figure 5B](#), [Figure S6](#)). The relative contribution of subset 2 end-members to bulk-sample composition is 81 and 16% ([Figure S6](#)).

Based on their similar characteristics, the two robust end-member loadings of both subsets are assigned the same subpopulations and named SF-EM1 and SF-EM2. Sediment assigned SF-EM1 dominates the sediment from

the more landward part of the marsh, whereas SF-EM2 is the main contributor to the coarser-grained sediments from close to the seaward edge of the marsh (see locations in [Figure 1E](#) and bar chart in [Figure 5B](#)).

End-member modelling results of core BT02 samples show a minimum number of two and a maximum number of four potential end-members ([Figure S3](#)). The first potential end-member show a clear mode at 20  $\mu\text{m}$ , whereas the others highly overlap, making it difficult to find the optimal number of end-members ([Figure S3](#)). The mean class-wise and sample-wise variances is slightly higher for a model with three end-members ( $R^2$  0.72 and 0.82) than for four end-members ( $R^2$  0.68 and 0.79). Based on this, three end-members were selected for core BT02. Grain-size class limits are 10–30, 50–80 and 80–150  $\mu\text{m}$  for end-members BT-EM1, BT-EM2 and BT-EM3, respectively. Modes are at 20, 68 and 93  $\mu\text{m}$

(Figure 5A), and the averaged relative contribution of end-members EM1, EM2 and EM3 to bulk-sample composition is 45%, 68% and 93%. Sediment attributed end-member BT-EM1 is dominant in the near-surface layers (0–15 cm) of core BT02 and in most samples from the interval 40–70 cm. End-member BT-EM3, by contrast, dominates the sediment composition between 15 and 25 cm, and at depths greater 70 cm.

Modelling results of core BT03 samples reveal a minimum number of two and a maximum number of six potential end-members (Figure S4). Three potential end-members overlap in the size range 70–160  $\mu\text{m}$  and are regarded as similar. The mean class-wise and sample-wise variances revealed highest values for three end-members ( $R^2$  0.73 and 0.89), with mode positions and cluster trends similar to core BT02 (Figures S3 and S4). Three end-members are therefore regarded as most likely. Grain-size class limits are 10–30, 60–80 and 80–150  $\mu\text{m}$  for end-members BT-EM1, BT-EM2 and BT-EM3, with dominant modes at 20, 57 and 93  $\mu\text{m}$  (Figure 5C,D). The relative contribution of the three end-members to the respective bulk-sample compositions is 32%, 34% and 34% (Figure S4). The portion of sediments assigned end-member BT-EM2 remains high throughout the core, whereas end-member BT-EM1 occurs predominantly in the lowermost and uppermost part of the succession (below 75 cm and above 20 cm). Contribution of sediments assigned BT-EM3 is variable in this core and visually correlates with sand layers.

To test for the stability of the analyses and to account for observed coast-normal gradients in grain size, all samples from Site 2 (cores BT02, BT03 and surface samples BT-SF) were pooled and considered for end-member modelling all together. This analysis again reveals three stable end-members BT-EM1<sub>pool</sub>, BT-EM2<sub>pool</sub> and BT-EM3<sub>pool</sub>, with respective modes at 20, 48 and 93  $\mu\text{m}$  (see Figure S1). Modes of BT-EM1<sub>pool</sub> and BT-EM3<sub>pool</sub> are identical to the modes of BT-EM1 (20  $\mu\text{m}$ ) and BT-EM3 (93  $\mu\text{m}$ ; Figure 5). The mode of BT-EM2<sub>pool</sub>, however, is slightly finer grained, if compared to the mode of BT-EM2 (57  $\mu\text{m}$ ) and the sediment portion attributed end-member BT-EM2<sub>pool</sub> increased in the pooled analysis and became dominant in both cores (Figure S1). This is interpreted to reflect the mixing of samples collected at different distances away from the marsh edge, that are deposited under different hydrodynamic conditions. The gradual fining of deposited grain-sizes with increasing distance from the marsh edge therefore results in a less sharp differentiation of grain-size populations in end-member modelling. Results of end-member modelling therefore appear sensitive against even subtle changes in the depositional conditions within the same sedimentary system.

Results for the recent storm-surge deposits remained comparable: Very similar to the site-specific analysis,

there are again only two end-members, BT-EM1<sub>pool</sub> and BT-EM2<sub>pool</sub> (Figure 5; Figure S1).

### 4.3 | Radioisotope data, age model and sedimentation rates

The cores show the expected exponential decrease of unsupported  $^{210}\text{Pb}$  activity with depth. However, cores BT02 and BT03 exhibit lower activities of unsupported  $^{210}\text{Pb}$  when compared to core RD04 (Figure 4). Radioisotope data from all cores allowed for age-model compilation.

#### 4.3.1 | Site 1, Rantum Dunes (core RD04)

Core RD04 shows a maximal total  $^{210}\text{Pb}$  activity of 8.25  $\text{DPM g}^{-1}$  (decays per minute per gram) in the uppermost section (0–2 cm below the surface), and a minimum of 0.20  $\text{DPM g}^{-1}$  at a depth of 31 cm (Figure 4A). Activity of unsupported  $^{210}\text{Pb}$  peaks with 7.7  $\text{DPM g}^{-1}$  in the uppermost sample and declines down to 0.91  $\text{DPM g}^{-1}$  at a depth of 26 cm (Figure 4A). A distinct second maximum occurs at a depth of 8 cm ( $^{210}\text{Pb}_{\text{unsupported}}$  6.4  $\text{DPM g}^{-1}$ ). Activity of  $^{137}\text{Cs}$  peaks at a depth of 22 cm (3.5  $\text{DPM g}^{-1}$ ). This maximum is assigned a depositional age of 1963 CE, assuming that this peak originates from atmospheric nuclear tests (Pennington et al., 1973).

The CRS model for core RD04 predicts a maximal sediment age of 81 years for a depth of 26 cm (Figure 4A); underlying sediments are assumed to be older than 130 years (6 half-lives of  $^{210}\text{Pb}$ ). These deeper sections were discarded from age-model compilation due to the rapid increase in DBD from 0.52 to 1.03  $\text{g cm}^{-3}$  below 26 cm depth (Figure 2). Errors of depositional ages range between  $\pm 1.7$  and  $\pm 10.2$  years (Figure 4).

Sedimentation rate at Site 1 (Rantum Dunes), as obtained from core RD04, varies between 2.7 and 7.8  $\text{mm year}^{-1}$  with a mean rate of 5.3  $\text{mm year}^{-1}$ . Marsh accretion was fastest around 1970 CE, in the 1980s CE, and past 2000 CE (Figure 6). Lowest sedimentation rates were found prior to 1960 CE and past 2010 CE. The CRS sediment accumulation rate was 0.13  $\text{g cm}^{-2} \text{ year}^{-1}$  on average and elevated during the 1970s CE and between 2005 and 2010 CE (see Figure S1).

Partitioning of bulk sedimentation rates show that the contribution of sediments assigned to end-members RD-EM1 and RD-EM2 remain small prior to 1955 CE and become dominant afterwards (Figure 6). The contribution of RD-EM3 sediments is highest in the 1940s CE (up to 3  $\text{mm year}^{-1}$ ), subsequently decreases until the mid-1970s CE, and remains at a low level until the early 2000s CE.



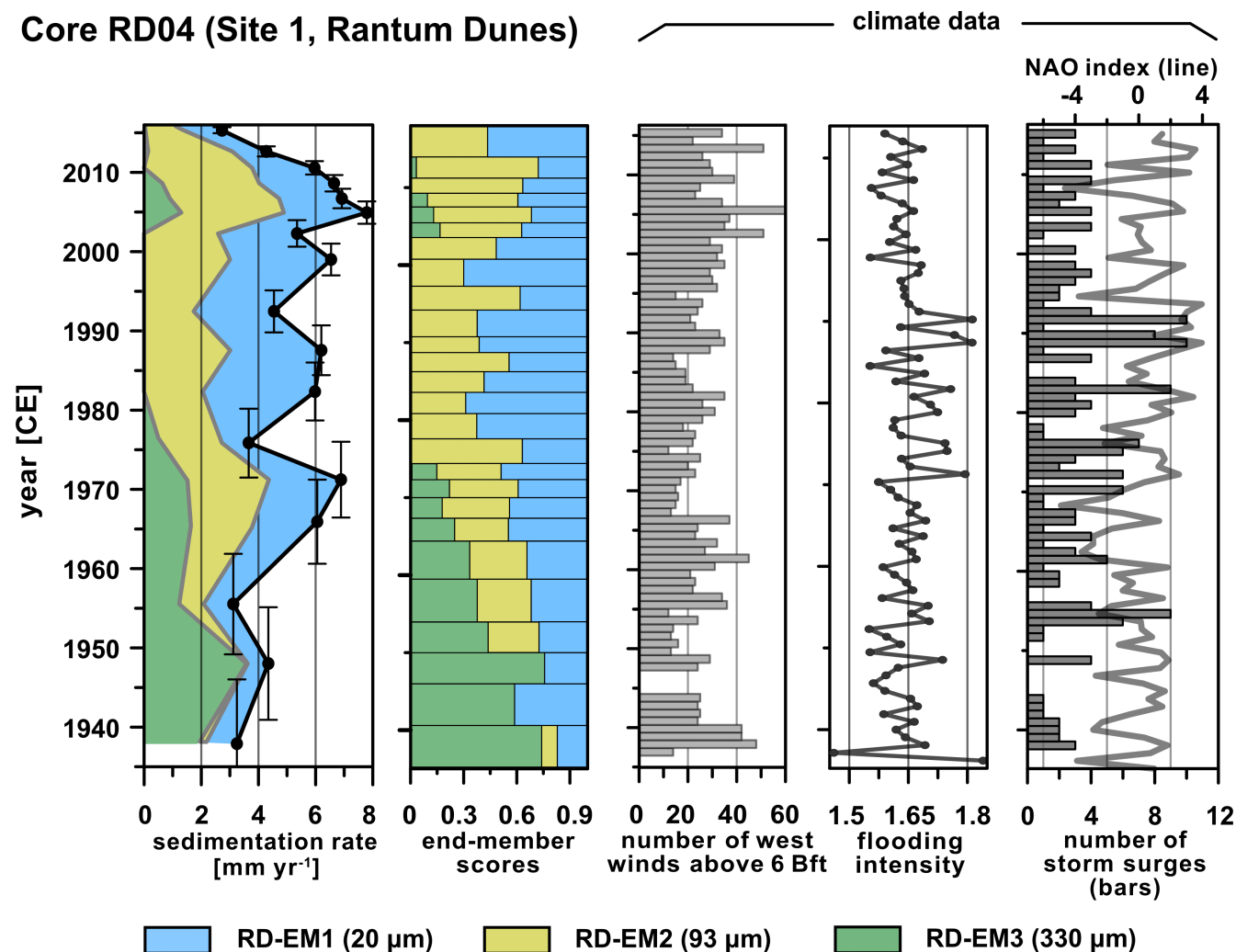


**FIGURE 6** Sedimentation rates and end-member modelling results of core BT04 (Site 1, Rantum Dunes) compared with meteorological and tide-gauge data. Note that sedimentation rates attributed to specific end-members are averaged over the respective time interval as determined by the age-model tie points.

During the first decade of the 21st century, contribution of RD-EM3 increases again (up to  $2.5 \text{ mm year}^{-1}$ ). Sediments assigned RD-EM4 are restricted to core depths not covered by the age model (Figure 2).

#### 4.3.2 | Site 2, Bay of Tümlau (cores BT02, BT03)

The total activity of  $^{210}\text{Pb}$  in core BT02 peaks with  $6.17 \text{ DPM g}^{-1}$  in the uppermost section (0–2 cm) and declines to  $0.59 \text{ DPM g}^{-1}$  at a depth of 90 cm (Figure 4B). The activity of unsupported  $^{210}\text{Pb}$  varies between 5.24 and  $0.39 \text{ DPM g}^{-1}$ , with maximal activity in the uppermost sample (Figure 4B). Core interval 8–18 cm shows a rapid decrease of  $^{210}\text{Pb}$  activity from 3.97 to  $0.64 \text{ DPM g}^{-1}$ ; whereas a constant rate of supply of unsupported  $^{210}\text{Pb}$  is assumed for the intervals 1–8 cm and

23–60 cm (compare methods section). The downcore  $^{210}\text{Pb}$  activity of core BT03, in contrast, shows no such break and activity of unsupported  $^{210}\text{Pb}$  decreases with depth ( $4.26$  to  $0.25 \text{ DPM g}^{-1}$ ) as expected (Figure 4C). In this core, background level of  $^{210}\text{Pb}$  is achieved below 60 cm. Activity of  $^{137}\text{Cs}$  in core BT02 has two peaks, at depths of 19 and 35 cm, with activity being higher at 19 cm. Based on this pattern, it is assumed that the upper  $^{137}\text{Cs}$  peak is caused by the Chernobyl reactor accident in 1986 CE (Aarkrog, 1988), whereas the lower peak most probably originates from fallout of atmospheric nuclear tests (Pennington et al., 1973). Both peaks in  $^{137}\text{Cs}$  activity also occur in core BT03, where peaks at 34 and 57 cm are assigned ages of 1986 and 1963 CE, respectively.

Two independent linear age models were assigned to core BT02 to account for the observed rapid decay of  $^{210}\text{Pb}$  between 8 and 18 cm core depth (Figure 4B; compare

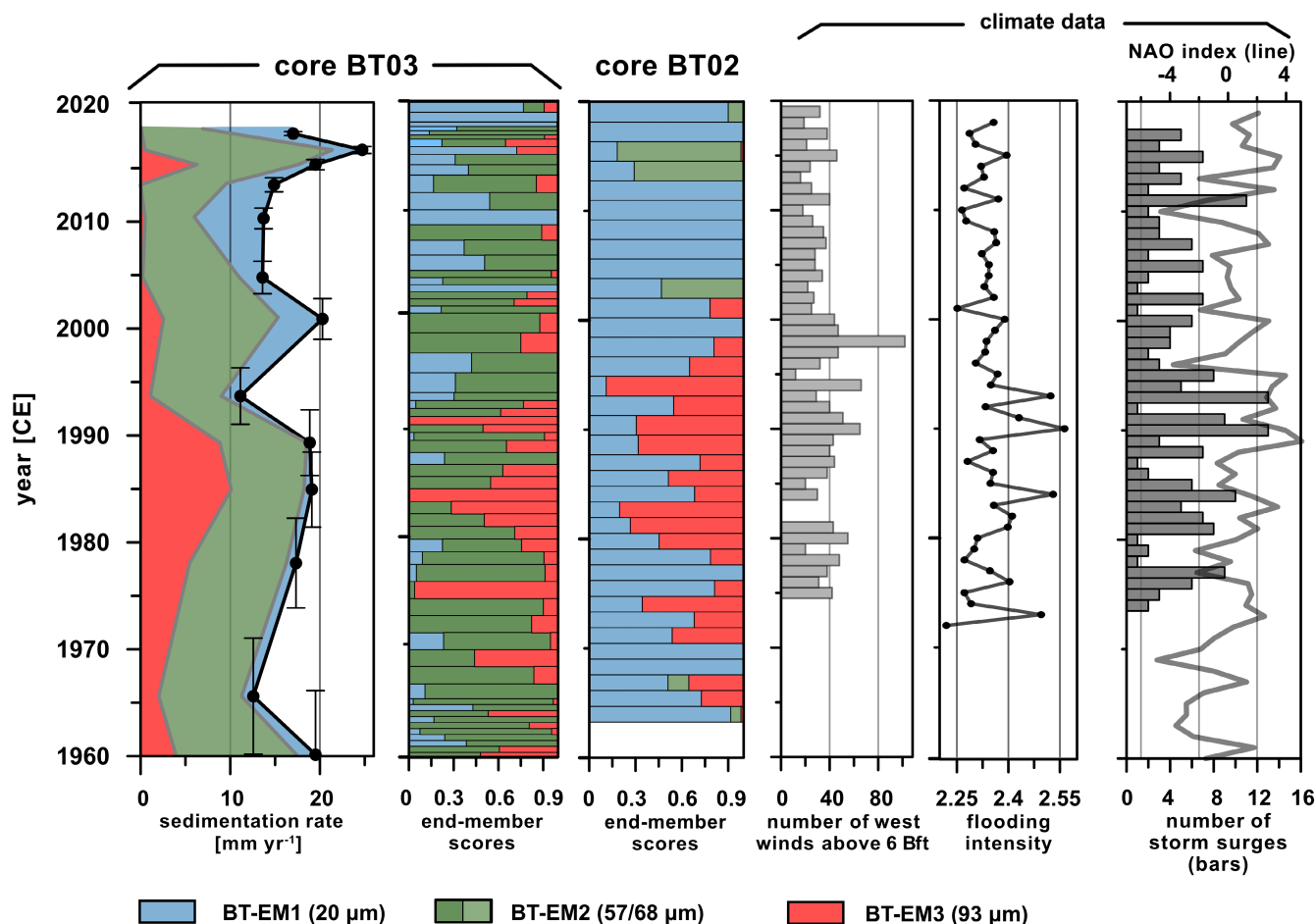


**FIGURE 7** Sedimentation rates and grain-size end-member modelling results of cores BT02 and BT03 (Site 2, Bay of Tümlau) compared with meteorological and tide-gauge data. Note that for core BT03, sedimentation rates attributed to specific end-members are averaged over the respective time interval as given by the age-model tie points.

methods section). Linear regression predicts a maximal age of 12 years for the upper interval (0–8 cm), and ages between 47 and 80 years for the lower interval (23–60 cm). Sections from below 60 cm in core BT02 were removed from age-model compilation as the background level in  $^{210}\text{Pb}$  activity has been achieved.

The CRS model for core BT03 gives a maximal age of 60 years corresponding to a core depth of 60 cm (Figure 4C). The sections below 60 cm were discarded from modelling, due to low unsupported  $^{210}\text{Pb}$  activity. As the  $^{210}\text{Pb}$  background level was not achieved at 60 cm depth, the CRS model was calibrated against the 1963 CE peak in  $^{137}\text{Cs}$ . The errors of sediment ages range between  $\pm 1.2$  and  $\pm 11.3$  years, with errors increasing with depth (Figure 4).

The split of the age model of core BT02 only allow for the calculation of linear sedimentation rates, which are  $11.2 \text{ mm year}^{-1}$  between 1963 and 1986 CE, and  $8.5 \text{ mm year}^{-1}$  between 1986 and 2020 CE. The overall sedimentation rate for core BT02 is  $9.7 \text{ mm year}^{-1}$ . Average sediment accumulation rates

are  $0.21 \text{ g cm}^{-2} \text{ year}^{-1}$  for the uppermost 8 cm, and  $0.82 \text{ g cm}^{-2} \text{ year}^{-1}$  for the depth interval 23–60 cm (see Figure S1). For core BT03, bulk sedimentation rate ranges between  $12.1$  and  $26.0 \text{ mm year}^{-1}$  with an overall mean of  $18.4 \text{ mm year}^{-1}$  (Figure 7). Sedimentation rate increases until 1990 CE (maximum  $18.9 \text{ mm year}^{-1}$ ). Subsequently, there is a low around the mid-1990s CE ( $11.1 \text{ mm year}^{-1}$ ), followed by peaks in 2000 CE ( $22.1 \text{ mm year}^{-1}$ ) and 2016 CE ( $26 \text{ mm year}^{-1}$ ). Between 2005 and 2014 CE, sedimentation rate remains below  $15 \text{ mm year}^{-1}$ . The mean CRS-based sediment accumulation rate for core BT03 is  $0.79 \text{ g cm}^{-2} \text{ year}^{-1}$ .

The contribution of sediments assigned to end-members BT-EM1 and BT-EM2 to marsh accretion at locality BT03 is  $9.0$ – $15.6 \text{ mm year}^{-1}$  and remains relatively constant between 1965 and 1990 CE (Figure 7). Subsequently, contribution of BT-EM1 slightly increases and is largest around 2010 CE. Relative contribution of sediments assigned to BT-EM3 to marsh surface elevation, by contrast, ranges between  $1.1$  and  $10.1 \text{ mm year}^{-1}$ , with highest rates in the mid-1980s CE.

## 4.4 | Climate and tide-gauge data

Data from tide-gauge Hörnum Hafen show an increase in the annual number of storm surges until the mid-1990s CE, and comparable low values afterwards (Figures 1 and 6). The marsh at Site 1 (Rantum Dunes) is inundated when water level reaches 1.35 m NHN (Figure 1C). Flooding intensity (annual mean inundation height) shows no clear trend, but appears slightly elevated in the time period 1970 to the early 1990s CE (Figure 6). In general, there is a positive correlation between the number of storm surges and the flooding intensity, as this has been observed elsewhere (Cid et al., 2015; Wahl, 2017). The occurrence of westerly winds exceeding 6 Bft ( $10.8 \text{ m s}^{-1}$ ) is elevated prior to 1940 CE, in the early 1960s CE, around 1980 CE, and past 1995 CE (Figure 6).

Data from tide-gauge Eider-Sperrwerk largely resemble the findings from Hörnum Hafen (Figures 1 and 7). They indicate a shortening of the storm-surge recurrence interval with time until 1990 CE. However, in comparison with Hörnum Hafen, station Eider-Sperrwerk registered more storm tides. Flooding intensity for the marsh at Site 2 (Bay of Tümlau) is elevated during the early 1990s CE, but shows no clear trend over the record. The number of westerly winds  $> 6$  Bft is elevated around 1990 and 2000 CE.

## 5 | DISCUSSION

### 5.1 | Sedimentology and rates of deposition

#### 5.1.1 | Site 1 (Rantum Dunes, core RD04)

Situated in a back-barrier setting, the marsh of Site 1 is sheltered from high-energy waves approaching from the open North Sea (Figure 1B). Marsh inundation during storm surges is consequently expected to represent comparable low-energy events without strong coastal wave activity. Such sedimentation under persistent low-energy conditions is reflected by the sediments of the upper 28 cm of core RD04 (Figure 2). These sediments are root-bearing, homogeneous, and fine-grained clay and silt, with a mean grain size of 16–33  $\mu\text{m}$  and less than 30% sand. There is an increase in organic content towards the modern surface, which is also seen in the radiographs as distinct light intervals (beds containing more organic matter). Sediments below 28 cm are sandy and have low organic content. Based on these findings, sediments in the upper 28 cm of core RD04 are interpreted as marsh deposits, whereas the underlying sands are tidal-flat deposits. The latter is corroborated by the textural similarity with the modern tidal-flat sediments in front of the marsh, which are also sandy (Puls et al., 2012). The transition from

intertidal to supra-tidal deposition is gradual (28–25 cm core depth) and characterised by an upward-decrease in sand content (95% to ~38%; Figure 2).

The aluminium–silicon ratio (Al/Si) of core RD04 sediments correlates with the mean grain size from spot sampling (correlation  $-0.70$ ;  $p < 0.05$ ; Figure 2). The Al/Si ratio is therefore regarded as a high-resolution proxy for grain-size changes, as this has been demonstrated in studies elsewhere (Din, 1992; Windom et al., 1989). The Al/Si data therefore allow for the identification of coarser-grained layers, which might be missed by discrete sampling and visual core description. In marshes elsewhere, such layers have been interpreted as storm deposits (Allen, 2000; Allen & Haslett, 2002; Castagno et al., 2021; Swindles et al., 2018; Wheeler et al., 1998). In core RD04 from the marsh of Rantum Dunes (Site 1) such layers are absent, corroborating assumed persistent low-energy sedimentation, even during storm surges (Figure 2).

The total carbon content in the uppermost 20 cm of core RD04 ranges from 8% to 15%, comparable to marshes in similar settings elsewhere (Chen et al., 2015; Sharma et al., 1987). As there are no mollusc shells, carbon content likely originates completely from plant productivity. Given a constant rate of plant productivity, beds with less organic carbon would reflect higher sedimentation rates, that is less time for soil formation, and vice versa. In this scenario, intervals with a lower organic content represent times of higher marsh-inundation frequency (Fagherazzi et al., 2012; Spohn et al., 2013). A higher temporal resolution of carbon content can be achieved using element ratios based on bromine, which is concentrated in organic matter and has been proven a reliable proxy for organic production (Caley et al., 2011; Mayer et al., 1981). Bromine–silicon (Br/Si) ratios from core RD04 indicate strong variations in organic content on the millimetre-scale, which correlate with carbon content obtained from spot samples (correlation 0.63;  $p < 0.05$ ).

Lead-210 activity in core RD04 shows the expected exponential decrease, and the CRS model predicts a maximum depositional age of 81 years for a depth of 26 cm below the modern marsh surface (Figures 4A and 6). Resulting sedimentation rate ranges from 2.7 to 7.8  $\text{mm year}^{-1}$ , with an average of 5.3  $\text{mm year}^{-1}$ . These sedimentation rates are in the same range as rates previously determined for the same marsh (Schuerch et al., 2012). Similar rates have been reported from comparable lagoonal back-barrier salt marshes elsewhere, like for example the marshes in Skallingen, Denmark (3–7.6  $\text{mm year}^{-1}$ ; Pedersen & Bartholdy, 2006) and the back-barrier salt marshes on the UK east coast (1–8  $\text{mm year}^{-1}$ ; French & Spencer, 1993). Based on these resemblances, the age model of core RD04 is seen to provide reliable depositional ages and sedimentation rates, which are representative for similar settings.

To summarise, marsh accretion at Site 1, Rantum Dunes, is seen to result from the accumulation of fine-grained sediment during low-energy inundation events, paired with a high rate of autochthonous marsh growth. Both processes show little fluctuations over the RD04 record.

### 5.1.2 | Site 2 (Bay of Tümlau, cores BT-02, BT03)

The marsh at Site 2 is located in an embayment, the Bay of Tümlau, whose entrance is partly barred with intertidal sandy shoals (Figure 1C). These shoals create a comparable calm environment during fair-weather conditions, but still allow storm waves to enter the bay during elevated water levels. Salt-marsh sediments of Site 2 lack any large shell fragments. This likely results from the comparable low-energy conditions in this part of the Bay of Tümlau, which prevent profound reworking of tidal flat deposits, even during storms. Sediment recovered in cores BT02 and BT03 is composed of clay and silt with intercalated sand layers (Figure 3). The sedimentary succession recovered in core BT02 is interpreted to completely represent marsh sediments. In core BT03, marsh sediments are present in the upper 73 cm, whereas sediments below are interpreted as intertidal deposits, based on the presence of lenticular bedding and textural similarities with the modern tidal flat surface in front of the marsh.

Sand layers intercalated into the finer-grained deposits are well imaged in the radiographs as dark layers. Their thickness ranges from one millimetre to several centimetres, and they are present predominantly in the lower parts of the cored successions. The mean grain size of the sand ranges between 60 and 89  $\mu\text{m}$ ; comparable to the surface sediment of the tidal flat in front of the marsh (mean grain size 44–89  $\mu\text{m}$ ; sand content up to 78%). Consequently, intercalated sand layers are seen to represent reworked sediment from the tidal flat, deposited under high-energy conditions, that is inundation of the marsh during storm surges (de Groot et al., 2011; Möller et al., 2014; Roman et al., 1997; Wheeler et al., 1998).

Total carbon content in cores BT02 and BT03 increases towards the surface and plant roots are present throughout the succession (Figure 3). This suggests an increase in autochthonous marsh growth with time (Bartholdy, 2012; Sullivan & Currin, 2002), which is also corroborated at higher resolution by the Br/Si ratios, tracing organic content (Figure 3). Marsh-soil development in the upper part of the cores is also seen in the radiographs where lighter layers correlate with higher organic contents (Figure 3). Conspicuous is the rapid increase in organics in the uppermost 15 cm of core BT02, which suggest a fast increase in plant productivity during the youngest period of marsh development, likely caused by the establishment of dense marsh vegetation.

In core BT02, the rapid increase of DBD from 0.35 to 0.7  $\text{g cm}^{-3}$  and the decrease of  $^{210}\text{Pb}$  activity from 4.9 to 1.39  $\text{DPM g}^{-1}$  in the upper interval (8–20 cm) suggests a hiatus. Sedimentological data, however, does not provide any indications for a break in sedimentation nor for erosion in this interval (Figures 3 and 4). It is therefore suggested that the shape of the down-core decay in unsupported  $^{210}\text{Pb}$  is caused by the incorporation of material that had lower  $^{210}\text{Pb}$  activity—likely due to reworking of older sediments. Such a reworking could result from a storm surge or from coastal management measures, like dredging and ditching. To account for the break in the  $^{210}\text{Pb}$  decay curve, the more reliable  $^{137}\text{Cs}$  marker horizons were used to set up a split, linear age model for core BT02 intervals 0–8 cm and 8–20 cm, respectively. Based on this, the CRS model predicts a maximum depositional age of 80 years at 60 cm core depth and is in good agreement with the  $^{137}\text{Cs}$  marker horizons (Figure 4).

Sedimentation rate at the locality of core BT02 is 11.2  $\text{mm year}^{-1}$  for the time period 1963–1986 CE and 8.5  $\text{mm year}^{-1}$  between 1986 and 2020 CE. In core BT03, sedimentation rate ranges between 12.1 and 26.0  $\text{mm year}^{-1}$  with an overall mean of 18.4  $\text{mm year}^{-1}$  (Figure 7). These data show that marsh accretion on the more landward part of the marsh (core BT02) is slower than on the seaward edge (core BT03), as expected due to the landward-dip of the marsh surface (Figure 1E).

High sedimentation rates, comparable to those at Site 2, are not uncommon for exposed marshes. Butzeck et al. (2015) for example reported sedimentation rates of up to 20.3  $\text{mm year}^{-1}$  from the brackish low marsh of the Elbe estuary. Such high rates of marsh accretion result from increased concentrations of sediments in the water column due to strong tidal currents and wave activity (Flor-Blanco et al., 2021; Möller et al., 2014; Murray et al., 1993; Vousdoukas et al., 2017; Yang et al., 2015) and consequently reflect the high-energy framework of exposed and semi-exposed marshes like the one of the Bay of Tümlau.

## 5.2 | Sediment provenance and depositional processes

Allochthonous sediment supply to marshes predominantly originates from inundation events, especially during storm surges (Möller et al., 2014; Morton, 1981; Stumpf, 1983; Yang et al., 2015). During such events, sediment is transported either in suspension or as traction load, sourced from the adjacent tidal flat as well as from lateral erosion of the marsh cliff (Rahman & Plater, 2014; Schuerch et al., 2019). Both modes of transport are expected to contribute to natural marsh growth in exposed, higher-energy settings, like the Bay of Tümlau. In sheltered, backbarrier settings, like



Rantum Dunes, suspension-based transport is expected to dominate. Here, coarse-grained sediment supply can arise from barrier overwash (Boldt et al., 2010; Neuhaus, 1994; Reineck & Gerdes, 1996; Warren & Niering, 1993), and potentially from aeolian transport.

### 5.2.1 | Low-energy, back-barrier salt marsh of Rantum Dunes (Site 1)

Core RD04 from the back-barrier marsh at Site 1 (Rantum Dunes) comprises homogeneous fine-grained sediment with little variations in grain-sizes (Figures 2 and 6). The setting makes the site prone to inundation during westerly storms, when water from the North Sea is pressed into the Hörnum Basin (Figure 1), as well as during easterly storms, when marsh inundation is caused by wind waves generated in the lagoon (fetch *ca* 20 km). End-member modelling of the grain-size distributions of core RD04 marsh sediments resulted in three robust end-member loadings RD-EM1, RD-EM2 and RD-EM3. A coarse-grained fourth end-member, RD-EM4, is restricted to the intertidal sediments underlying the marsh (Figures 2 and 5A).

The finest-grained end-member, RD-EM1 (mode at 20  $\mu\text{m}$ ), is restricted to the salt-marsh sediments (upper 28 cm; Figure 2). Dominated by particles in the clay and fine-silt range, it is proposed that this end-member comprises the sediment portion settled from suspension load during marsh inundation. Such accumulation of fine-grained sedimentation on marsh surfaces is predominantly controlled by marsh vegetation, which acts as a sediment trap and reduces flow velocity (Fagherazzi et al., 2013; Rahman & Plater, 2014; Stumpf, 1983).

End-member RD-EM2 (mode 93  $\mu\text{m}$ ) is also restricted to the salt-marsh sediments. Contribution of RD-EM2 to bulk sediment is smaller compared to the finer-grained RD-EM1. A partitioning of finer and coarser-grained material is typical for low salt marshes and is interpreted to reflect different transport mechanisms (Rahman & Plater, 2014). The decrease in transport energy with increasing distance to the marsh edge usually results in a gradual fining of the sediment towards the land. For core RD04, it is proposed that sediments assigned end-member RD-EM2 were transported as traction load, whereas the finer-grained material of RD-EM1 settled from suspension load.

End-member RD-EM3 (mode 330  $\mu\text{m}$ ) contributes to sediments throughout the core, including salt-marsh as well as intertidal deposits (Figures 2 and 6). There is a variability with time and RD-EM3 becomes less prominent in sediments deposited between 1938 and 1975 CE, and is almost absent in the youngest part of the succession (Figure 6). Sandy deposits on marshes are in general interpreted as deposited by storm surges (de Groot et al., 2011;

Roman et al., 1997; Stumpf, 1983; Swindles et al., 2018), when sand from adjacent tidal flats is relocated onto the marsh (de Groot et al., 2011; van Straaten, 1954). It fits with this interpretation that sediments assigned to RD-EM3 (mean grain size 330  $\mu\text{m}$ ) exhibit similar grain sizes as sediments of the adjacent intertidal areas (between 310 and 408  $\mu\text{m}$ ; Park, 1974). However, the up-core decrease of RD-EM3 is not paralleled by any of the hydrological parameters (flooding intensity, storm surge frequency; Figure 6). This indicates a decoupling of marsh inundation and the deposition of sediments assigned to RD-EM3 and makes storm deposition of the sandy component less likely. Overwash deposition, another potential mechanism of coarse-grained sediment supply to back-barrier marshes, usually results in sharp-based distinct sand layers (Boldt et al., 2010; Ehlers et al., 1993), sedimentary features completely missing in core RD04 (Figure 2).

As an alternative interpretation, sediments assigned to RD-EM3 are suggested to represent aeolian-transported sand from the dunes that cover the barrier landward (westward) of the studied marsh (Figures 1B and 8A). These dunes are composed of medium sand (mean grain size 350–500  $\mu\text{m}$ ; Tillmann & Wunderlich, 2013). Sediments assigned to RD-EM3 (mean 330  $\mu\text{m}$ ) could therefore represent a sub-population of dune sediments, generated by transport fractionation. Potential paths for aeolian sediment transport are the west–east striking interdune valleys westward of the studied marsh (Figure 8A). The dominance of westerly winds in the study area (Lindhorst & Reimann, 2021; Nehls & Thiel, 1993) facilitates sand export from the dunes towards the marsh and further into the back-barrier lagoon (Goldschmidt et al., 1993). Dunes are therefore seen as a likely source of the sand fraction represented by end-member RD-EM3 in core RD04.

Further evidence for aeolian sediment supply to the marsh of Rantum Dunes comes from historical aerial and satellite imagery of the area, which shows an increase in vegetation coverage of the dunes with time (Figure 8B). Aeolian sediment transport on dunes is sensitive to the presence of vegetation, and become restricted and even suppressed if vegetation coverage increases (Osswald et al., 2019). The image acquired in the year 1958 CE shows numerous areas with open sand on the dunes westward of the Site 1 marsh (Figure 8B). These areas decreased in size afterwards but are still visible on the image obtained in 1972 CE. The expansion of vegetated areas parallels the decrease in the portion of RD-EM3 sediments in core RD04 during the same time period (Figure 6). Subsequently, between the years 1972 and 1999 CE, dunes became completely covered with vegetation; synchronous with this time period was a reduction in the contribution of sediments assigned to end-member RD-EM3 to negligible amounts. The slight increase in RD-EM3 sediments

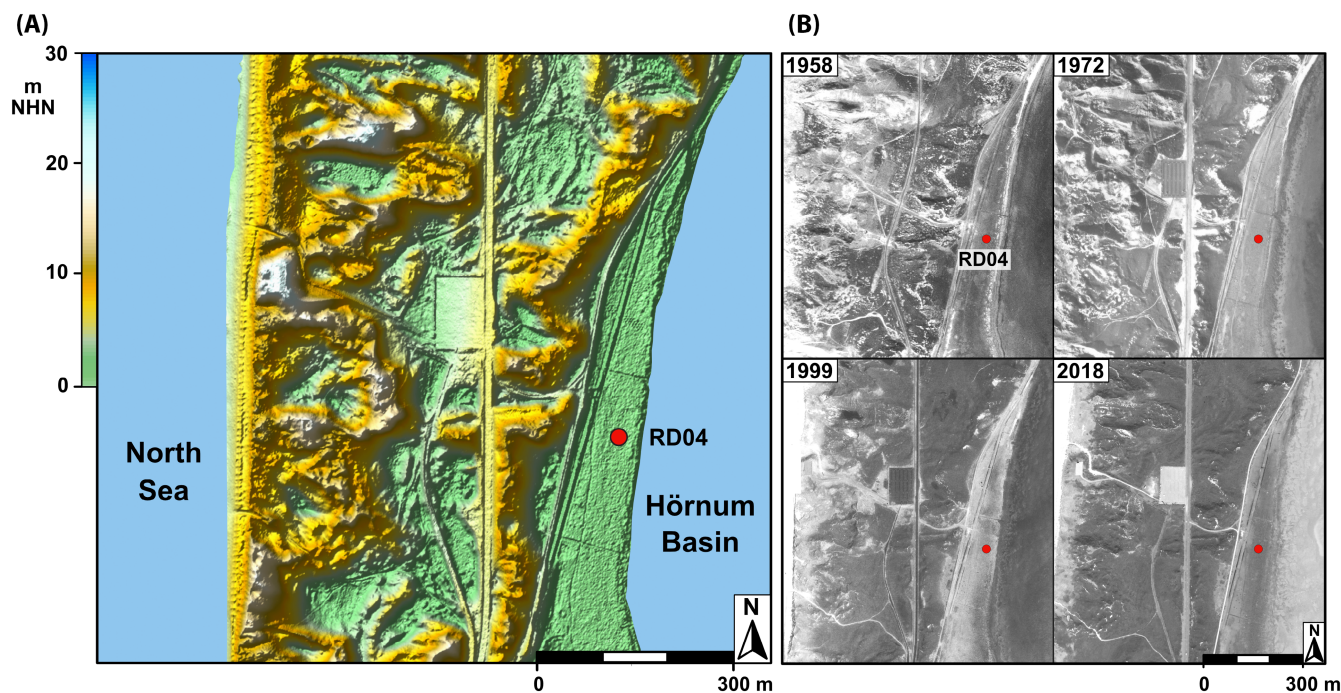


**FIGURE 8** Topography of Site 1 (Rantum Dunes; see Figure 1 for location) and historical development of vegetation coverage. (A) Digital elevation model based on LIDAR data obtained in the year 2002. Data provided by the LKN.SH (Husum, Germany); (B) Historical aerial images (years 1958, 1972, 1999 CE) and satellite imagery (2018 CE). Light to dark-grey colours indicates vegetation coverage, white areas are open sand. Note increase of vegetation coverage with time. Red dot: position of core RD04.

between 2002 and 2010 CE, however, cannot be explained with changes in dune vegetation, but could result from an increase in the frequency of westerly winds during the same time (Figure 6), which potentially deliver sand from the western shore (ca 0.5 km away; Figure 1).

Quantification of the relative contribution of RD-EM3 to bulk sediment composition shows that aeolian-transported sediment accounts for marsh accretion at Rantum Dunes in the range of  $3 \text{ mm year}^{-1}$  in the late-1940s and  $>1 \text{ mm year}^{-1}$  afterwards, until 1970 CE (Figure 6). For two decades (between 1980 and 2000 CE), aeolian sediment supply was almost non-existent, but resumed in the early 2000s CE and reaches  $2.5 \text{ mm year}^{-1}$  around 2005 CE. Based on these data, aeolian sediment supply is regarded as a previously underestimated component of marsh growth in back-barrier settings and alone results in marsh-accretion rates able to outpace the long-term sea-level rise in the study area ( $1.6 \text{ mm year}^{-1}$  for the time period 1900–2011; Wahl et al., 2013 and higher rates of up to  $3.6 \text{ mm year}^{-1}$  for the recent decades; Dangendorf et al., 2012; Steffelbauer et al., 2022).

To summarise, three processes are seen to contribute to marsh accretion at Rantum Dunes (Figure 9A): During marsh inundation, fine-grained sediment settles from suspension (end-member RD-EM1) or is transported as traction load (RD-EM2). Suspension-load derived sediments accounts for  $0.7\text{--}3.5 \text{ mm year}^{-1}$  of marsh accretion; traction load contributed  $0.1\text{--}3.6 \text{ mm year}^{-1}$  (in total

$23.0\text{--}97.3\%$  of marsh growth). A proposed third agent of sediment supply to the marsh is aeolian sediment transport (RD-EM3). This wind-derived material is coarser and contributes between  $0.1$  and  $3.0 \text{ mm year}^{-1}$  to marsh accretion ( $2.7\text{--}77.0\%$  of marsh accretion).

## 5.2.2 | High-energy marsh of the Bay of Tümlau (Site 2)

### 5.2.2.1 | Recent storm surge deposits (surface samples)

Samples of storm surge deposited material, collected from the marsh surface at Site 2 revealed two robust grain-size end-member loadings, namely SF-EM1 and SF-EM2 (Figure 5B, Figures S5 and S6). The finer-grained SF-EM1 (mode around  $20 \mu\text{m}$ ) is dominant in samples from more landward localities of the marsh (subset 2), whereas the coarser-grained SF-EM2 (mode  $68 \mu\text{m}$ ) dominates samples from the more seaward part (subset 1). This resembles a source-to-sink differentiation in grain size, from the seaward marsh edge towards their landward termination, similar to marshes elsewhere (Collins et al., 1987; Yang et al., 2008). Lateral trends in grain-size over marshes are interpreted as caused by marsh vegetation, which reduces flow velocity and enhances deposition and trapping of suspension load towards the landward side of the marsh (Fagherazzi et al., 2013; Leonard & Croft, 2006;

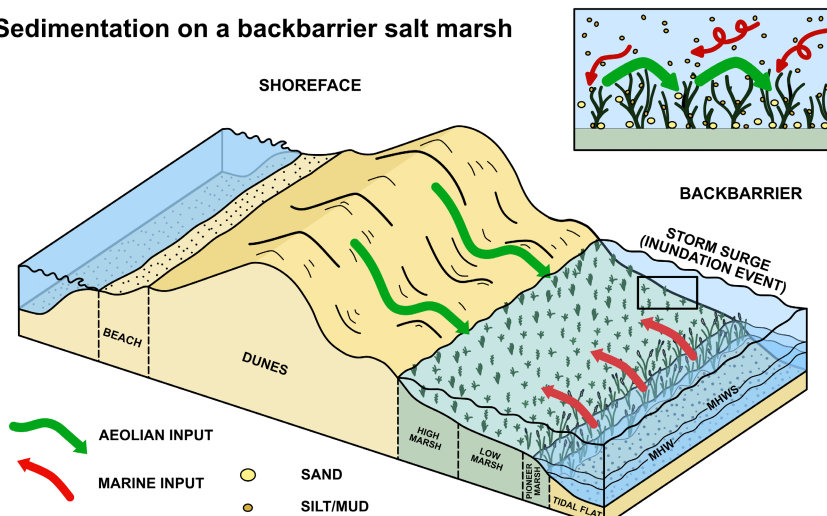
Mudd et al., 2010; Stumpf, 1983). Consequently, sediments assigned to end-member SF-EM1 are interpreted to resemble material settled from suspension load, whereas sediments assigned to SF-EM2 are assumed to be transported as traction load.

#### 5.2.2.2 | Cores BT02 and BT03

End-member analysis of grain-size data from core BT03 resulted in three robust end-members BT-EM1, BT-EM2 and BT-EM3 (Figures 5D). Recovered from the more seaward part of the marsh, sediment of core BT03 is expected to be dominated by material transported as traction load. This view is corroborated by the predominance of end-member BT-EM2 (mode 57  $\mu\text{m}$ ), which is very similar to end-member SF-EM2 (mode 68  $\mu\text{m}$ ) from the recent storm-surge deposits. Consequently, sediment assigned to end-member BT-EM2 represent the main component of flood deposition near the marsh edge (Figures 9B).

The finer-grained BT-EM1 (mode 20  $\mu\text{m}$ ) exhibits similar loading properties as SF-EM1 from the storm surge deposits. Corresponding material in core BT03 is therefore seen to originate from suspension load during inundation. The portion of these sediments slightly increases towards the top of the core, past 2000 CE, but remains on a low level. This relative increase in suspension load with time likely results from the establishment of a high marsh around 2000 CE (Müller-Navarra et al., 2019; Stock et al., 2005); a stage in marsh development characterised by dense vegetation, which more effectively traps sediment from suspension (Fagherazzi et al., 2013). The associated elevation of the marsh platform also leads to a long-term decrease of inundation (Allen, 2000; Bartholdy et al., 2004), which further reduces effective transport energy—a self-amplifying process. Both effects, establishment of high-marsh vegetation and elevation of the marsh platform, can explain the decrease in the rate of

#### Sedimentation on a backbarrier salt marsh



#### Sedimentation on an exposed setting

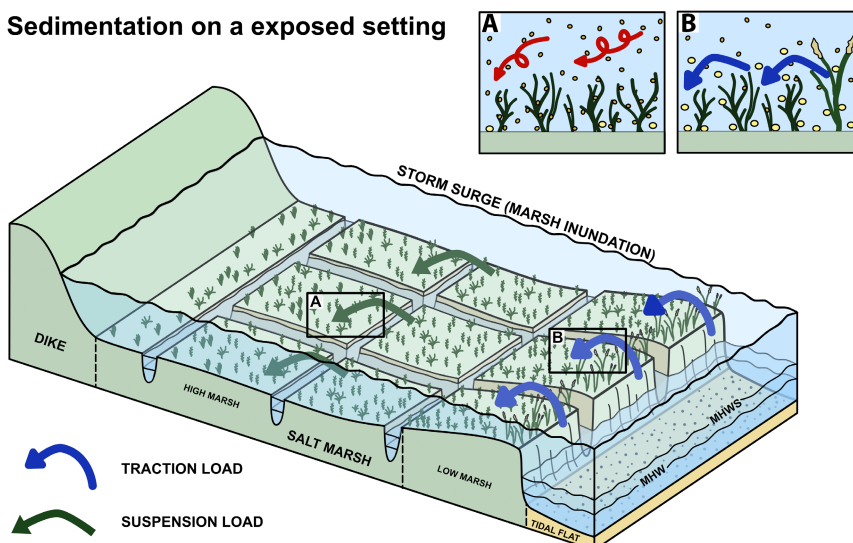


FIGURE 9 Simplified sedimentary model summarising the morphological characteristics of the marshes and the sedimentary transport processes involved. (A) Site 1, Rantum Dunes; and (B) Site 2, Bay of Tümlau. See text for discussion of the depositional processes involved.



sedimentation at Site BT03 during the early 21st century (from 20 to 12 mm year<sup>-1</sup>).

The sediment portion assigned to end-member BT-EM3 is a fine sand (Figure 5) comparable to the surface sediments of the adjacent tidal flat (mean grain size 44–89 μm). This makes it plausible that BT-EM3 sediments were transported from the tidal flat onto the marsh during storm surges. This view is corroborated by tide gauge data, which show that end-member BT-EM3 is more prominent, when storm-surge frequency and flooding intensity are elevated, like for example in the 1980s, and the early 1990s CE (Figure 7). With this in mind, it appears likely that coarse-grained BT-EM3 sediments originate from severe storm surges. Nevertheless, end-member BT-EM3 is completely missing in the surface samples collected after the storm surge in February 2012 from the same salt marsh.

An alternative explanation for the origin of the BT-EM3 sediments is seen in coastal defence measures. Material deposited in the marsh drainage channels (the ditches) is excavated and dispersed onto the salt-marsh surface (a process called ‘ditching’). Sediments in marsh channels are generally coarser than sediments on the marsh surface, likely the result of higher flow velocities in the channels, especially during marsh inundation (Allen, 1996; French & Stoddart, 1992). Marsh channels are therefore a potential source of coarse sediment, like the sediment fraction BT-EM3. This is corroborated by the sedimentary record: Sediments assigned to BT-EM3 were predominantly deposited prior to 2000 CE, that is in times when the marsh was managed. Ditching took place every 3–7 years and was terminated in 1998 CE (Müller-Navarra et al., 2016; Stock et al., 2005). Regarding the uncertainty of the age model ( $\pm 3.5$  years in this time interval), this is in good agreement with the last occurrence of BT-EM3 sediments in core BT02 and a strong decrease of BT-EM3 in core BT03 (Figure 7). A link between coastal defence measures and the input of coarser material to the marshes on Site 2 is also corroborated by a previous study on cores from the same marsh, which, based on foraminiferal associations, suggested that sandy intervals with grain-size characteristics similar to BT-EM3 result from ditching (Müller-Navarra et al., 2019).

Partitioning of total marsh accretion rates with respect to sediment portions assigned to the different end-members of core BT03 shows that the natural sediment accretion (the combination of suspension load and traction load) ranges from 9.0 to 15.6 mm year<sup>-1</sup> and remains largely constant throughout the core (Figure 7). The variability in bulk-sedimentation rate (0.2–10.1 mm year<sup>-1</sup>) therefore mainly results from variable input of sediments attributed to BT-EM3, eventually reflecting coastal defence measures. These sediments alone contributed between 1.1 and 10.1 mm year<sup>-1</sup> to net marsh accretion at Site 2.

### 5.3 | Climate signals in the sedimentary succession of marshes

The grain size of salt-marsh sediments closely resembles the flow strength during transport and deposition (Allen, 2000; Christiansen et al., 2000). This makes marshes potential recorders of storm climate. The correlation of instrumental time series of wind and bulk-sediment derived proxy data, however, often remains ambiguous, likely due to the multiplicity of sedimentary processes involved. This especially applies to managed marshes, where the sedimentary signature of natural control is masked by anthropogenic measures, and the sedimentary record of climate therefore is biased. Further restrictions to the reconstruction of climate records from marshes comes from their limited temporal resolution, which is due to post-sedimentary bioturbation and compaction of their sediments. The effect of bioturbation on the record of events, like single storms, is obvious in salt marshes, where the preservation of storm-deposited sand layers inversely correlates with layer thickness and is afflicted with high spatial inhomogeneity (Hippensteel, 2008; Swindles et al., 2018). This explains why the frequency of storm events reconstructed from sediments decreases with time and is often much lower if compared to instrumental and historical records (Hippensteel, 2008, 2010). Bearing this in mind, marshes are expected to provide climate records on multi-decadal to decadal timescales but are far from allowing reconstructions on the event scale.

To test for the potential of marsh sediments as an archive of supra-regional storminess, grain-size data and end-member modelling results are compared with the NAO. For westerly exposed marshes, like the Bay of Tümlau, sediments are expected to become coarser when storm activity is increased; that is the NAO is positive. For back-barrier marshes, like Rantum Dunes, however, where sedimentation takes place under low-energy conditions and inundation also occurs during easterly storms, the link to supra-regional patterns in storm climate is expected to be less clear.

The correlation coefficient of bulk mean grain size of core BT03 sediments with the NAO index (Hurrell, 1995) is 0.16 ( $p < 0.05$ ) (dashed blue curve in Figure 10B). This correlation remains at a low level (0.14;  $p < 0.05$ ) even if a peak-to-peak fit is attempted within the error range of the age model (red curve in Figure 10B). The latter indicates that the weak correlation between the grain size of marsh sediments at Site 2 (Bay of Tümlau) and the NAO is not the result of uncertainties in the age model. Instead, it is hypothesised that episodic marsh management introduced a certain bias to the data series. To test this, bulk-sediment portions potentially attributed to ditching



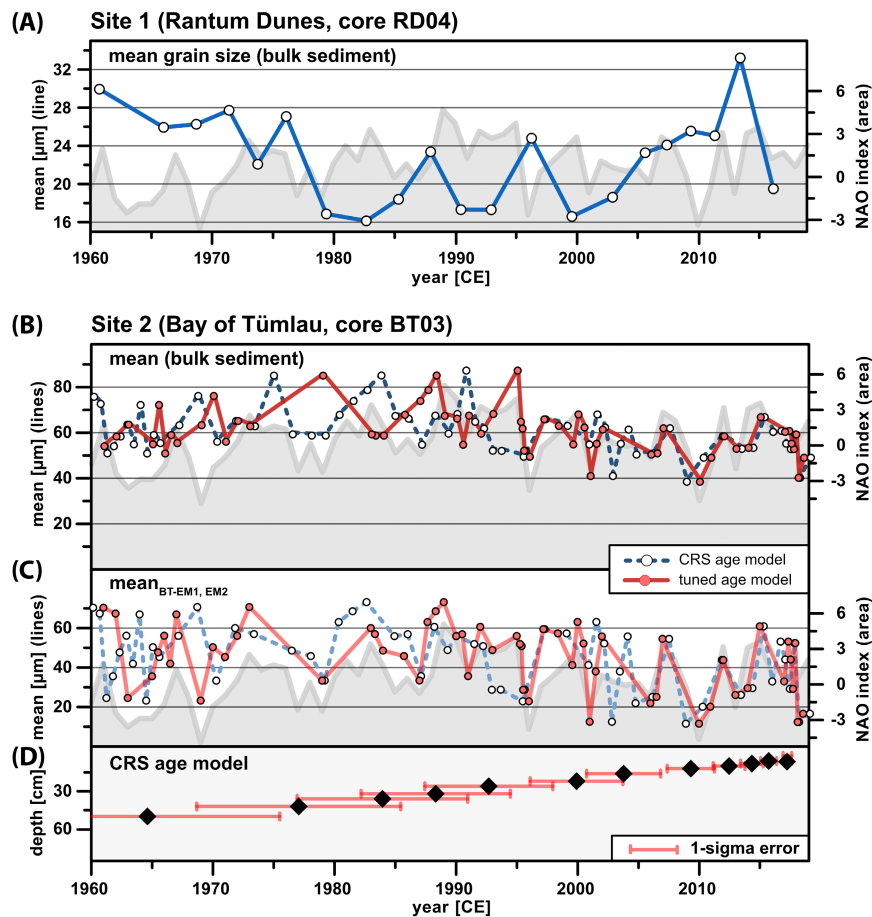


**FIGURE 10** Comparison of grain-size data and the North Atlantic Oscillation index (NAO; data are from Hurrell & National Center for Atmospheric Research Staff, 2020). (A) Bulk mean grain size of core RD04 sediments (Site 1, Rantum Dunes) and NAO data (grey line). (B) Mean grain size of core BT03 (Site 2, Bay of Tümlau). Dashed blue line: Data plotted using the CRS age model (D); red line: data plotted using a modified age model, obtained by peak-to-peak correlation of grain-size and NAO data (grey line) within the error range of the age model. See text for details; (C) Mean grain size of the sediment portion attributed to natural transport processes (end-members BT-EM1 and -EM2). For explanation of line styles see (B); (D) CRS age model for core BT03 with error ranges.

(end-member BT-EM3, grain-size limits 80–150  $\mu\text{m}$ ) were excluded from the analysis, and grain-size statistics were re-calculated for the remaining grain-size spectrum. This data is assumed to comprise only sediments deposited by natural processes during marsh inundation (end-members BT-EM1 and BT-EM2, representing suspension load and traction load, respectively). In doing so, the correlation of mean grain size (now mean  $_{\text{BT-EM1, EM2}}$ ) and NAO is 0.10 ( $p < 0.05$ ) by using the original age model (dashed blue line in Figure 10C). Correlation, however, improves to 0.55 ( $p < 0.05$ ) if a peak-to-peak fit within the error range of the age model is achieved (Figure 10D; red line in Figure 10C).

At Site 1 (Rantum Dunes), marsh accretion past 1970 CE primarily results from settling of fines under low-energy conditions during storm surges, whereas older sediments contain a significant coarse-grained component, likely derived from aeolian input (Figures 6 and 9). The correlation of core RD04 mean grain size and NAO is  $-0.3$  ( $p < 0.05$ ; Figure 10A). This negative correlation potentially reflects increased mobilisation of fine-grained material in the lagoon during stormier periods. The assumed increase of aeolian input past 2000 CE (Figure 6) likely causes a decoupling of NAO and deposited grain size for younger times and masks the NAO-controlled variability in the fine fraction.

## 6 | CONCLUSIONS

Sediment supply to back-barrier marshes is dominated by the settling of fine-grained material transported in suspension during inundation. Sediment transported as traction load is present in these marshes, but plays a minor role in marsh accretion due to the low-energy framework conditions. In addition, aeolian transport of sand from nearby dunes can significantly enhance vertical marsh growth, alone outpacing the rate of present sea-level rise. By contrast, salt-marsh accretion in more exposed settings is controlled by higher-energy transport that comprises traction and suspension load. On the seaward side of such marshes, sedimentation is mainly controlled by traction load, whereas further landward, settling of suspension load prevails— even during storm surges. Sediments of these marshes are coarser-grained compared to back-barrier marshes and accretion rates are higher. Marshes in both settings seem to be able to keep pace with present sea-level rise—even without anthropogenic marsh management.

End-member modelling of grain-size distributions provides a method to determine and quantify the sedimentary processes that control marsh accretion. This includes the identification of sedimentary traces of anthropogenic measures in managed marshes.

Marshes are potential recorders of storm climate. The correlation of grain-size sub-populations (end-members) with supra-regional climate variability on decadal time scales imply that even managed marshes allow for the extraction of climate signals as long as natural and anthropogenic processes are determined and their relative contribution is quantified. Data series based solely on bulk sediment samples, by contrast, seem to be of limited use due to the potential overprint of natural processes by marsh management. Data also show that the validation of marsh-derived records with meteorological time series is a question of time scales; and proxy-records with temporal resolutions exceeding decadal time-scales are unlikely to be achieved from marshes.

### ACKNOWLEDGEMENTS


We acknowledge financial support by the Deutsche Forschungsgemeinschaft (DFG) for the project “SEASTORM” (Li2005/2-1 and 2-2) within the DFG Priority Program SPP1889 ‘Regional Sea Level Change and Society (SeaLevel)’. Jutta Richarz (Uni Hamburg) and Sascha Plewe (IOW) are thanked for laboratory analyses; Dirk Eggers and Benjamin Eberhardt for field assistance. Xiaoxi Hu from Flett Research, Canada, is thanked for making the radioisotope measurements. The Landesbetrieb Küstenschutz (LKN) in Husum, Germany, is thanked for providing the aerial images and LIDAR data used in Figure 8, and the work permit for the natural protection area in Sylt. The Wasserstraßen- und Schifffahrtsamt Tönning, Germany is thanked for providing tide-gauge data; and the National Park Schleswig-Holsteinisches Wattenmeer for providing permissions to work in the salt marshes of Eiderstedt peninsula.

### DATA AVAILABILITY STATEMENT

Grain-size data for cores RD04, BT02, BT03, as well as the surface samples are provided in the supplementary materials. Results of radionuclide measurements and XRF data can be found at the data depository PANGAEA (doi:10.1594/PANGAEA.933869 and 10.1594/PANGAEA.933896).

### ORCID

Nina Lenz  <https://orcid.org/0000-0001-9617-212X>

Sebastian Lindhorst  <https://orcid.org/0000-0001-9615-4167>

### REFERENCES

- Aarkrog, A. (1988) The radiological impact of the Chernobyl debris compared with that from nuclear weapons fallout. *Journal of Environmental Radioactivity*, 6, 151–162.
- Allen, J.R.L. (1995) Salt-marsh growth and fluctuating sea-level: implications of a simulation model for Holocene coastal stratigraphy and peat-based sea-level curves. *Sedimentary Geology*, 100, 21–45.
- Allen, J.R.L. (1996) Shoreline movement and vertical textural patterns in salt marsh deposits: implications of a simple model for flow and sedimentation over salt marshes. *Proceedings of the Geologists' Association*, 107, 15–23.
- Allen, J.R.L. (2000) Morphodynamics of Holocene salt marshes: a review sketch from the Atlantic and southern North Sea coasts of Europe. *Quaternary Science Reviews*, 19, 1155–1231.
- Allen, J.R.L. & Haslett, S.K. (2002) Buried salt-marsh edges and tidal-level cycles in the mid-Holocene of the Caldicot Level (Gwent), South Wales, UK. *The Holocene*, 12, 303–324.
- Allen, J.R.L. & Pye, K. (1992) Coastal salt marsh: their nature and importance. In: Allen, J.R.L. & Pye, K. (Eds.) *Salt marshes: morphodynamics, conservation and engineering significance*. London: Cambridge University Press, pp. 1–18.
- Andersen, T.J., Svinth, S. & Pejrup, M. (2011) Temporal variation of accumulation rates on a natural salt marsh in the 20th century – the impact of sea level rise and increased inundation frequency. *Marine Geology*, 279, 178–187.
- Appleby, P.G., Richardson, N., Nolan, P.J. & Oldfield, F. (1990) Radiometric dating of the United Kingdom SWAP sites. *Philosophical Transactions of the Royal Society of London*, 327, 233–238.
- Aranda, M., Gracia, F. J., Peralta, G., and Flor-Blanco, G. (2020) The Application of high-resolution mapping for the analysis of recent eco-geomorphological changes in the saltmarshes of San Vicente de la Barquera Estuary (North Spain). *Journal of Coastal Research*, 95(SI), 341–345.
- Avnimelech, Y., Ritvo, G., Meijer, L.E. & Kochba, M. (2001) Water content, organic carbon and dry bulk density in flooded sediments. *Aquacultural Engineering*, 25, 25–33.
- Bartholdy, J. (2012) Salt marsh sedimentation. In: Davis, R., Jr. & Dalrymple, R. (Eds.) *Principles of tidal sedimentology*. Dordrecht: Springer, pp. 151–185.
- Bartholdy, J., Christiansen, C. & Kunzendorf, H. (2004) Long term variations in backbarrier saltmarsh deposition on the Skallingen peninsula – the Danish Wadden Sea. *Marine Geology*, 203, 1–21.
- Bartholdy, J., Pedersen, J.B.T. & Bartholdy, A.T. (2010) Autocompaction of shallow silty salt marsh clay. *Sedimentary Geology*, 223, 310–319.
- Besonen, M. (2012) Marsh coring—portable, rapid, and perfect core recovery. Available from: <http://esslab.tamucc.edu/tools-marsh-coring.html> [Accessed 24 August 2022].
- Binford, M.W. (1990) Calculation and uncertainty analysis of <sup>210</sup>Pb dates for PIRLA project lake sediment cores. *Journal of Paleolimnology*, 3, 253–267.
- Blott, S.J. & Pye, K. (2001) GRADISTAT: a grain size distribution and statistics package for the analysis of unconsolidated sediments. *Earth Surface Processes and Landforms*, 26, 1237–1248.
- Boldt, K.V., Lane, P., Woodruff, J.D. & Donnelly, J.P. (2010) Calibrating a sedimentary record of overwash from southeastern New England using modelled historic hurricane surges. *Marine Geology*, 275, 127–139.
- Boorman, L.A., Garbutt, A. and Barratt, D. (1998) The role of vegetation in determining patterns of the accretion of salt marsh sediment. In: Black, K.S., Paterson, D.M. and Cramp, A. (Eds.) *Sedimentary processes in the intertidal zone*, Special Publication 139. Geological Society, London, pp. 389–399.

- Bunzel, D., Milker, Y., Müller-Navarra, K., Arz, H.W. & Schmiedl, G. (2021) North Sea salt-marsh archives trace past storminess and climate variability. *Global and Planetary Change*, *198*, 103403.
- Butzeck, C., Eschenbach, A., Grongroft, H.K., Nolte, S. & Jensen, K. (2015) Sediment deposition and accretion rates in tidal marshes are highly variable along estuarine salinity and flooding gradient. *Estuaries and Coasts*, *38*, 434–450.
- Caley, T., Malaizé, B., Zaragosi, S., Rossignol, L., Bourget, J., Eynaud, F., Martinez, P., Giraudeau, J., Charlier, K. & Ellouzi-Zimmerman, N. (2011) New Arabian Sea records help decipher orbital timing of Indo-Asian monsoon. *Earth and Planetary Science Letters*, *308*, 433–444.
- Castagno, K.A., Tomiczek, T., Shepard, C.C., Beck, M.W., Bowden, A.A., O'Donnell, K. & Scyphers, D.B. (2021) Resistance, resilience, and recovery of salt marshes in the Florida Panhandle following Hurricane Michael. *Scientific Reports*, *11*, 20381.
- Chen, Y., Chen, G. & Ye, Y. (2015) Coastal vegetation invasion increases greenhouse gas emission from wetland soils but also increases soil carbon accumulation. *Science of the Total Environment*, *526*, 19–28.
- Christiansen, T., Wiberg, P.L. & Milligan, T.G. (2000) Flow and sediment transport on a tidal salt marsh surface. *Estuarine, Coastal and Shelf Science*, *50*, 315–331.
- Cid, A., Menéndez, M., Castanedo, S., Abascal, A.J., Méndez, F.J. & Medina, R. (2015) Long-term changes in the frequency, intensity and duration of extreme storm surge events in southern Europe. *Climate Dynamics*, *46*, 1503–1516.
- Collins, L.M., Collins, J.N. & Leopold, L.B. (1987) Geomorphic processes of an estuarine marsh: preliminary hypotheses. *International Geomorphology*, *1*, 1049–1072.
- Dangendorf, S., Wahl, T., Hein, H., Jensen, J., Mai, S. & Mudersbach, C. (2012) Mean sea level variability and influence of the North Atlantic oscillation on long-term trends in the German Bight. *Water*, *4*, 170–195.
- de Groot, A.V., Veeneklaas, R.M. & Bakker, J.P. (2011) Sand in the salt marsh: contribution of high-energy conditions to salt-marsh accretion. *Marine Geology*, *282*, 240–254.
- Dietze, E. & Dietze, M. (2019) Grain-size distribution unmixing using the R package EMMAgeo, Eiszeitalter und Gegenwart. *Quaternary Science Journal*, *68*, 29–46.
- Dietze, E., Hartmann, K., Diekmann, B., IJmker, J., Lehmkuhl, F., Opitz, S., Stauch, G., Wünnemann, B. & Borchers, A. (2012) An end-member algorithm for deciphering modern detrital processes from lake sediments of Lake Donggi Cona, NE Tibetan Plateau, China. *Sedimentary Geology*, *243–244*, 169–180.
- Dietze, E., Maussion, F., Ahlborn, M., Diekmann, B., Hartmann, K., Henkel, K., Kasper, T., Locket, G., Opitz, S. & Habertzettl, T. (2014) Sediment transport processes across the Tibetan Plateau inferred from robust grain-size end members in lake sediments. *Climate of the Past*, *10*, 91–106.
- Dietze, M. and Dietze, E. (2016) EMMAgeo: end-member modelling of grain-size data. Available from: <https://cran.r-project.org/web/packages/EMMAgeo/> [Accessed 24 August 2022].
- Dietze, M., Schulte, P. & Dietze, E. (2021) Application of end-member modelling to grain-size data: constraints and limitations. *Sedimentology*, *69*, 845–863.
- Dijkema, K.S. (1987) Geography of salt marshes in Europe. *Zeitschrift für Geomorphologie*, *31*, 489–499.
- Din, T.B. (1992) Use of aluminium to normalize heavy-metal data from estuarine and coastal sediments of Straits of Melaka. *Marine Pollution Bulletin*, *24*, 484–491.
- Duarte, C.M., Dennison, W.C., Orth, R.J.W. & Carruthers, T.J.B. (2008) The charisma of coastal ecosystems: addressing the imbalance. *Estuaries and Coasts*, *31*, 233–238.
- Dypvik, H. & Harris, N.B. (2001) Geochemical facies analysis of fine-grained siliciclastics using Th/U, Zr/Rb and (Zr + Rb)/Sr ratios. *Chemical Geology*, *181*, 131–146.
- Ehlers, J., Nagorny, K., Schmidt, P., Stieve, B. & Zietlow, K. (1993) Storm-surge deposits in North-Sea salt marshes dated by Cs-134 and Cs-137 determination. *Journal of Coastal Research*, *9*, 698–701.
- Fagherazzi, S., Kirwan, M.L., Mudd, S.M., Guntenspergen, G.R., Temmerman, S., D'Alpaos, A., Van de Koppel, J., Rybczyk, J.M., Reyes, C.C. & Clough, J. (2012) Numerical models of salt marsh evolution: ecological, geomorphic, and climatic factors. *Reviews of Geophysics*, *50*, RG1002.
- Fagherazzi, S., Wiberg, P.L., Temmerman, S., Struyf, E., Zhao, Y. & Raymond, P.A. (2013) Fluxes of water, sediments, and biogeochemical compounds in salt marshes. *Ecological Processes*, *3*, 1–16.
- Flor-Blanco, G., Alcántara-Carrió, J., Jackson, D.W.T., Flor, G. & Flores-Soriano, C. (2021) Coastal erosion in NW Spain: recent patterns under extreme storm wave events. *Geomorphology*, *387*, 107767.
- Folk, R.L. & Ward, W.C. (1957) Brazos River bar: a study in the significance of grain size parameters. *Journal of Sedimentary Research*, *27*, 3–26.
- French, J.R. (1993) Numerical simulation of vertical marsh growth and adjustment to accelerated sea-level rise, North Norfolk, U.K. *Earth Surface Processes and Landforms*, *18*, 63–81.
- French, J.R. & Spencer, T. (1993) Dynamics of sedimentation in a tide-dominated backbarrier salt marsh, Norfolk, UK. *Marine Geology*, *110*, 315–331.
- French, J.R. & Stoddart, D.R. (1992) Hydrodynamics of salt marsh creek systems: implications for marsh morphological development and material exchange. *Earth Surface Processes and Landforms*, *17*, 235–252.
- Friedman, G.M. (1967) Dynamic processes and statistical parameters compared for size frequency distribution of beach and river sands. *Journal of Sedimentary Petrology*, *37*, 327–354.
- Goldberg, E.D. (1963) Geochronology with <sup>210</sup>Pb. In: *Radioactive dating*. Vienna: International Atomic Energy Agency, pp. 121–227.
- Goldschmidt, P., Bayerl, K.A., Austen, I. & Köster, R. (1993) From the Wanderdünen to the Watt: coarse-grained aeolian sediment transport on Sylt, Germany. *Zeitschrift für Geomorphologie*, *37*, 171–178.
- Goodbred, S.L. & Hine, A.C. (1995) Coastal storm deposition: salt-marsh response to a severe extratropical storm, March 1993, West-Central Florida. *Geology*, *23*, 679–682.
- Hayes, M.O. (1979) Barrier island morphology as a function of tidal and wave regime. In: Leatherman, S.P. (Ed.) *Barrier islands from the Gulf of St. Lawrence to the Gulf of Mexico*. New York: Academic Press, pp. 1–27.
- Hippensteel, S.P. (2008) Preservation potential of storm deposits in South Carolina back-barrier marshes. *Journal of Coastal Research*, *24*, 594–601.
- Hippensteel, S.P. (2010) Paleotempestology and the pursuit of the perfect paleostorm proxy. *GSA Today*, *20*, 52–53.
- Hofstede, J.L.A. (1997) Morphologie des St. Peter-Ordung-Sandes. *Die Küste*, *59*, 143–172.



- Hurrell, J.W. & National Center for Atmospheric Research Staff (2020) Hurrell North Atlantic Oscillation (NAO) Index (station-based). Available from: <https://climatedataguide.ucar.edu/climate-data/hurrell-north-atlantic-oscillation-nao-index-station-based> [Accessed 24 August 2022].
- Hurrell, J.W. (1995) Decadal trends in the North Atlantic oscillation: regional temperatures and precipitation. *Science*, *269*, 676–679.
- Hurrell, J.W., Kushnir, Y., Ottersen, G. and Visbeck, M. (2003) An overview of the North Atlantic oscillation. In: Hurrell, J.W., Kushnir, Y., Ottersen, G., Visbeck, M. and Visbeck M.H. (Eds.) *The North Atlantic Oscillation: climatic significance and environmental impact, Geophysical Monograph Series*, vol. 134. Washington, DC: American Geophysical Union, pp. 1–35.
- Kelletat, D. (1992) Coastal erosion and protection measures at the german North Sea coast. *Journal of Coastal Research*, *8*, 699–711.
- Kirwan, M. & Temmerman, S. (2009) Coastal marsh response to historical and future sea-level acceleration. *Quaternary Science Reviews*, *28*, 1801–1808.
- Kirwan, M.L., Guntenspergen, G.R., D'Alpaos, A., Morris, J.T., Mudd, S.M. & Temmerman, S. (2010) Limits on the adaptability of coastal marshes to rising sea level. *Geophysical Research Letters*, *37*, L23401.
- Kirwan, M.L. & Megonigal, P. (2013) Tidal wetland stability in the face of human impacts and sea-level rise. *Nature*, *504*, 53–60.
- Kolker, A.S., Goodbred, S.L., Jr., Hameed, S. & Cochran, J.K. (2009) High-resolution records of the response of coastal wetland systems to long-term and short-term sea-level variability. *Estuarine, Coastal and Shelf Science*, *84*, 493–508.
- Lamprecht, H.O. (1957) Uferveränderung und Küstenschutz auf Sylt. *Die Küste*, *6*, 39–93.
- Leonard, L.A. & Croft, A.L. (2006) The effect of standing biomass on flow velocity and turbulence in Spartina alterniflora canopies. *Estuarine, Coastal and Shelf Science*, *69*, 325–336.
- Leonardi, N. & Fagherazzi, S. (2014) How waves shape salt marshes. *Geology*, *42*, 887–890.
- Li, J., Vandenbergh, J., Mountney, N.P. & Luthi, S.M. (2020) Grain-size variability of point-bar deposits from a fine-grained dryland river terminus, Southern Altiplano, Bolivia. *Sedimentary Geology*, *403*, 105663.
- Lindhorst, S. & Betzler, C. (2016) The climate-archive dune: sedimentary record of annual wind intensity. *Geology*, *44*, 711–714.
- Lindhorst, S., Betzler, C. & Hass, H.C. (2008) The sedimentary architecture of a Holocene barrier spit (Sylt, German Bight): swash-bar accretion and storm erosion. *Sedimentary Geology*, *206*, 1–16.
- Lindhorst, S. & Reimann, T. (2021) Sedimentary architecture, genesis, and implications for palaeo-climate reconstructions. *Earth Surfaces Processes and Landforms*, *46*, 2177–2194.
- Mariotti, G. & Fagherazzi, S. (2010) A numerical model for the coupled long-term evolution of salt marshes and tidal flats. *Journal of Geophysical Research: Earth Surface*, *115*, F01004.
- Mayer, L.M., Macko, S.A., Mook, W.H. & Murray, S. (1981) The distribution of bromine in coastal sediments and its use as a source indicator for organic matter. *Organic Geochemistry*, *3*, 37–42.
- Patterson, R.T., Mazzella, V., Macumber, A.L., Gregory, B.R.B., Patterson, C.W., Nasser, N.A., Roe, H.M., Galloway, J.M. & Reinhardt, E.G. (2020) A novel protocol for mapping the spatial distribution of storm derived sediment in lakes. *SN Applied Sciences*, *2*, 1–16.
- McFadden, L., Spencer, T. & Nicholls, R.J. (2007) Broad-scale modelling of coastal wetlands: what is required? *Hydrobiologia*, *577*, 5–15.
- Meier, D. (2004) Man and environment in the marsh area of Schleswig-Holstein from Roman until late Medieval times. *Quaternary International*, *112*, 55–69.
- Möller, I. (2006) Quantifying saltmarsh vegetation and its effect on wave height dissipation: results from a UK East coast saltmarsh. *Estuarine, Coastal and Shelf Science*, *69*, 337–351.
- Möller, I., Kudella, M., Rupprecht, F., Spencer, T., Paul, M., van Wesenbeeck, B., Wolters, K., Jensen, G., Bouma, K., Miranda-Lange, T.J. & Schimmels, M.S. (2014) Wave attenuation over coastal salt marshes under storm surge conditions. *Nature Geoscience*, *7*, 727–731.
- Morris, J.T., Sundareshwar, P.V., Nietch, C.T., Kjerfve, B. & Cahoon, D.R. (2002) Responses of coastal wetlands to rising sea level. *Ecology*, *83*, 2869–2877.
- Morton, R.A. (1981) Formation of storm deposits by wind-forced currents in the Gulf of Mexico and the North Sea. *Special Publications of the International Association of Sedimentologists*, *5*, 385–396.
- Mudd, S.M., D'Alpaos, A. & Morris, J.T. (2010) How does vegetation affect sedimentation on tidal marshes? Investigating particle capture and hydrodynamic controls on biologically mediated sedimentation. *Journal of Geophysical Research: Earth Surface*, *115*, F03029.
- Müller-Navarra, K., Milker, Y., Bunzel, D., Lindhorst, S., Friedrich, J., Arz, H.W. & Schmiedl, G. (2019) Evolution of a salt marsh in the southeastern North Sea region – anthropogenic and natural forcing. *Estuarine, Coastal and Shelf Science*, *218*, 268–277.
- Müller-Navarra, K., Milker, Y. & Schmiedel, G. (2016) Natural anthropogenic influence on the distribution of salt marsh foraminifera in the bay of Tümlau, German North Sea. *The Journal of Foraminifera Research*, *46*, 61–74.
- Murray, S.P., Walker, N.D. & Adams, C. (1993) Impacts of winter storms on sediment transport within the Terrebonne Bay marsh complex. In: Laska, S. & Puffer, A. (Eds.) *Coastlines of the Gulf of Mexico*. New Orleans: American Society of Civil Engineers, pp. 56–70.
- Nehls, G. & Thiel, M. (1993) Large-scale distribution patterns of the mussel *Mytilus edulis* in the Wadden Sea of Schleswig-Holstein: do storms structure the ecosystem? *Netherlands Journal of Sea Research*, *31*, 181–187.
- Neuhaus, R. (1994) Mobile dunes and eroding salt marshes. *Helgoländer Meeresuntersuchungen*, *48*, 343–358.
- Oldfield, F., Wake, R., Boyle, J., Jones, R., Nolan, S., Gibbs, Z., Appleby, P., Fisher, E. & Wolff, G. (2003) The late Holocene history of Gormire Lake (NE England) and its catchment: a multiproxy reconstruction of past human impact. *The Holocene*, *13*, 677–690.
- Osswald, F., Dolch, T. & Reise, K. (2019) Remobilizing stabilized island dunes for keeping up with sea level rise? *Journal of Coastal Conservation*, *23*, 675–687.
- Park, Y.A. (1974) (Table 1) Grain size parameters of intertidal channel sand bars near Sylt. North-Frisian Wadden Sea: PANGAEA. <https://doi.org/10.1594/PANGAEA.783271>
- Pedersen, J.B.T. & Bartholdy, J. (2006) Budgets for fine-grained sediment in the Danish Wadden Sea. *Marine Geology*, *235*, 101–117.
- Pennington, W., Cambay, R.S. & Fisher, E.M. (1973) Observations on lake sediments using fallout <sup>137</sup>Cs as a tracer. *Nature*, *242*, 324–326.



- Pethick, J.S. (1981) Long-term accretion rates on tidal salt marshes. *Journal of Sedimentary Research*, *51*, 571–577.
- Pittauerova, D., Hettwig, B. & Fischer, H.W. (2011) Pb-210 sediment chronology: focused on supported lead. *Radioprotection*, *46*, 277–282.
- Puls, W., van Bernem, K.H., Eppel, D., Kapitzka, H., Pleskachevsky, A., Riethmüller, R. & Vaessen, B. (2012) Prediction of benthic community structure from environmental variables in a soft-sediment tidal basin (North Sea). *Helgoland Marine Research*, *66*, 345–361.
- Rahman, R. & Plater, A.J. (2014) Particle-size evidence of estuary evolution: a rapid and diagnostic tool for determining the nature of recent saltmarsh accretion. *Geomorphology*, *213*, 139–152.
- Reed, D.J. (1989) Patterns of sediment deposition in subsiding coastal salt marshes, Terrebonne Bay, Louisiana: the role of winter storms. *Estuaries*, *12*, 222–227.
- Reed, D.J. (1990) The impact of sea-level rise on coastal salt marshes. *Progress in Physical Geography*, *14*, 465–481.
- Reed, D.J. (1995) The response of coastal marshes to sea-level rise: survival or submergence? *Earth Surface Processes and Landforms*, *20*, 39–48.
- Reineck, H.E. & Gerdes, G. (1996) A seaward prograding siliciclastic sequence from upper tidal flats to salt marsh facies (southern North Sea). *Facies*, *34*, 209–218.
- Roman, C.T., Peck, J.A., Allen, J.R., King, J.W. & Appleby, P.G. (1997) Accretion of a New England (USA) salt marsh in response to inlet migration, storms, and sea-level rise. *Estuarine, Coastal and Shelf Science*, *45*, 717–727.
- Schuerch, M., Rapaglia, J., Liebetrau, V., Vafeidis, A. & Reise, K. (2012) Salt marsh accretion and storm tide variation: an example from a barrier island in the North Sea. *Estuaries Coasts*, *35*, 486–500.
- Schuerch, M., Spencer, T. & Evans, B. (2019) Coupling between tidal mudflats and salt marshes affects marsh morphology. *Marine Geology*, *412*, 95–106.
- Sharma, P., Gardner, L.R., Moore, W.S. & Bollinger, M.S. (1987) Sedimentation and bioturbation in a salt marsh as revealed by  $^{210}\text{Pb}$ ,  $^{137}\text{Cs}$ , and  $^7\text{Be}$  studies. *Limnology and Oceanography*, *32*, 313–326.
- Spohn, M., Babka, B. & Giani, L. (2013) Changes in soil organic matter quality during sea-influenced marsh soil development at the North Sea coast. *Catena*, *107*, 110–117.
- Steffelbauer, D.B., Riva, R.E.M., Timmermann, J.S., Kwakkel, J.H. & Bakker, M. (2022) Evidence of regional sea-level rise acceleration for the North Sea. *Environmental Research Letters*, *17*, 074002.
- Stevenson, J.C. & Kearney, M.S. (2009) Impacts of global climate change and sea-level rise on tidal wetlands. In: Silliman, B.R., Grosholz, E.D. & Bertness, M.D. (Eds.) *Human impacts on salt marshes: a global perspective*. Berkeley: University of California Press, pp. 171–206.
- Stock, M., Gettner, S., Hagge, H., Heinzl, K., Kohlus, J. & Stumpe, H. (2005) Salzwiesen an der Westküste von Schleswig-Holstein 1988–2001. *Schriftenreihe des Nationalparks Schleswig-Holsteinisches Wattenmeer*, *15*, 240.
- Stumpf, R.P. (1983) The process of sedimentation on the surface of a salt marsh. *Estuarine, Coastal and Shelf Science*, *17*, 495–508.
- Sullivan, M.J. & Currin, C.A. (2002) Community structure and functional dynamics of benthic microalgae in salt marshes. In: Weinstein, M.P. & Kreeger, D.A. (Eds.) *Concepts and controversies in tidal marsh ecology*. Dordrecht: Kluwer Academic, pp. 81–106.
- Swindles, G.T., Galloway, J.M., Macumber, A.L., Croudace, I.W., Emery, A.R., Woulds, C., Bateman, M.D., Parry, L., Jones, J.M., Selby, K., Rushby, G.T., Baird, A.J., Woodroffe, S.A. & Barlow, N.L.M. (2018) Sedimentary records of coastal storm surges: evidence of the 1953 North Sea event. *Marine Geology*, *403*, 262–270.
- Tillmann, T. & Wunderlich, J. (2013) Barrier rollover and spit accretion due to the combined action of storm surge induced washover events and progradation: insights from ground-penetrating radar surveys and sedimentological data. *Journal of Coastal Research*, *SI65*, 600–605.
- van Hoang, L., Clift, P.D., Schwab, A.M., Huuse, M., Nguyen, D.A. & Zhen, S. (2010) Large-scale erosional response of SE Asia to monsoon evolution reconstructed from sedimentary records of the Song Hong-Yinggehai and Qiongdongnan basins, South China Sea. *Geology Society London Special Publications*, *342*, 219–244.
- van Straaten, L.M.J.U. (1954) Composition and structure of recent marine sediments in the Netherlands. *Leidse Geologische Mededelingen*, *19*, 1–110.
- Vauclin, S., Mourier, B., Dendievel, A.-M., Noclin, N., Piégay, H., Marchand, P., Vénisseau, A., de Vismes, A., Lefèvre, I. & Winiarski, T. (2021) Depositional environments and historical contamination as a framework to reconstruct fluvial sedimentary evolution. *Science of The Total Environment*, *764*, 142900.
- Vousdoukas, M.I., Mentaschi, L., Voukouvalas, E., Verlaan, M. & Feyen, L. (2017) Extreme sea levels on the rise along Europe's coasts. *Earth's Future*, *5*, 304–323.
- Wahl, T. (2017) Sea-level rise and storm surges, relationship status: complicated! *Environmental Research*, *12*, 111001.
- Wahl, T., Haigh, I., Albrecht, F., Dillingh, D., Jensen, J., Nicholls, R., Weisse, R., Woodworth, P.L. & Wöppelmann, G. (2013) Observed mean sea level changes around the North Sea coastline from 1800 to present. *Earth Science Reviews*, *124*, 51–67.
- Wahl, T., Jensen, J. & Frank, T. (2010) On analysing sea level rise in German Bight since 1844. *Natural Hazards and Earth System Sciences*, *10*, 171–179.
- Warren, R.S. & Niering, W.A. (1993) Vegetation change on a north-east tidal marsh: interaction of sea-level rise and marsh accretion. *Ecology*, *74*, 96–103.
- Weltje, G.J. (1997) End-member modeling of compositional data: numerical-statistical algorithms for solving the explicit mixing problem. *Mathematical Geology*, *29*, 503–549.
- Weltje, G.J. & Prins, M.A. (2003) Muddled or mixed? Inferring palaeoclimate from size distributions of deep-sea clastics. *Sedimentary Geology*, *162*, 39–62.
- Weltje, G.J. & Prins, M.A. (2007) Genetically meaningful decomposition of grain-size distributions. *Sedimentary Geology*, *202*, 409–424.
- Wheeler, A.J., Orford, J.D. & Dardis, O. (1998) Saltmarsh deposition and its relationship to coastal forcing over the last century on the north-west coast of Ireland. *Geologie en Mijnbouw – Netherlands Journal of Geosciences*, *77*, 295–310.
- Windom, H.L., Schropp, S.J., Calder, F.D., Ryan, D.J., Smith, R.G., Burney, L.C., Lewis, F.G. & Rawlinson, C.H. (1989) Natural trace metal concentrations in estuarine and coastal marine

- sediments of the southeastern United States. *Environmental Science and Technology*, 23, 314–320.
- Wohlenberg, E. (1953) Sinkstoff, Sediment und Anwachs am Hindenburgdamm. *Küste*, 2, 33–91.
- Wolff, W.J., Bakker, J.P., Laursen, K. and Reise, K. (2010) The Wadden Sea quality status report – synthesis Report 2010. Wadden Sea Ecosystem, 29, Common Wadden Sea Secretariat, Wilhelmshaven, pp. 25–74.
- Yang, F., Karius, V. & Sauer, D. (2020) Quantification of loess proportions in Pleistocene periglacial slope deposits and Holocene colluvium using grain-size data sby laser diffractometry. *Journal of Plant Nutrition and Soil Science*, 183, 277–281.
- Yang, J., Graf, T. & Ptak, T. (2015) Sea level rise and storm surge effects in a coastal heterogeneous aquifer: a 2D modelling study in northern Germany. *Grundwasser*, 20, 39–51.
- Yang, S.L., Li, H., Bouma, T.J., Zhang, W.X., Wang, Y.Y., Li, P., Li, M. & Ding, P.X. (2008) Spatial and temporal variations in sediment grain size in tidal wetlands, Yangtze delta: on the role of physical and biotic controls. *Estuarine, Coastal and Shelf Science*, 77, 657–671.
- Zar, J.H. (2005) Spearman rank correlation. In: *Encyclopedia of Biostatistics*. New York: John Wiley & Sons, Ltd. <https://doi.org/10.1002/0470011815.b2a15150>

## SUPPORTING INFORMATION

Additional supporting information can be found online in the Supporting Information section at the end of this article.

**How to cite this article:** Lenz, N., Lindhorst, S. & Arz, H. W. (2023). Determination and quantification of sedimentary processes in salt marshes using end-member modelling of grain-size data. *The Depositional Record*, 9, 4–29. <https://doi.org/10.1002/dep2.213>